Two-color-driven enhanced high-order harmonic generation in solids

Francisco Navarrete and Uwe Thumm
Department of Physics, Kansas State University, Manhattan, Kansas 66506, USA

(Received 11 October 2020; accepted 11 December 2020; published 29 December 2020)

We theoretically investigate the emission of high-harmonic (HH) radiation in model crystals by bichromatic few-cycle driving pulses that are composed as the phase-coherent superposition of a mid-infrared fundamental pulse and its second harmonic. Adjusting the model-crystal parameters to reproduce the lowest band gap of MgO, we examine the extent to which distinct domains of the HH spectrum can be controlled and enhanced by tuning the temporal profile of the bichromatic driving laser electric field. We change the driving-pulse shape by varying its fundamental-versus-second-harmonic pulse amplitude ratio and delay, while keeping the energy of the driving laser pulse fixed. For suitable amplitude ratios and delays, we find an up to fivefold enhancement of the spectral HH yield and significant shifts of the HH cutoff frequency.

DOI: 10.1103/PhysRevA.102.063123

I. INTRODUCTION

Exposed to an intense multicycle driving laser pulse, atomic, molecular, and solid targets emit radiation at multiples of the driving frequency in a process referred to as high-order harmonic generation (HHG). For gaseous media, HHG has been extensively studied over the past three decades and is well understood as a three-step mechanism involving tunneling ionization, acceleration, and recombination of the active electron in the electric field of the driving laser pulse [1–6]. While solids have been scrutinized theoretically, for about an equal period of time, as possible targets for generating more intense high-harmonic (HH) radiation than gaseous targets, owing to their much larger electron density [7–10], HHG in solids by intense infrared (IR) laser pulses has been confirmed experimentally two decades later [11]. In contrast to HHG from gases, the theoretical description of solid HHG remains a matter of intense debate [12–16]. HH spectra from solids and gases were found to be qualitatively distinct, the main differences being the scaling of the HH cutoff frequency with the driving laser field strength (linear for solid as opposed to quadratic for gaseous HHG) [11,12,14,17,18], the existence of multiple plateaus in HH spectra from solids [12,19], and the influence of the external-field-driven (dynamical) joint density of states [20].

HHG in gases is the fundamental process in the generation of attosecond light pulses, which are currently employed in a large number of experiments capable of probing diverse aspects of the electronic dynamics in gaseous and solid matter with attosecond resolution in time (see Refs. [21–25] and references therein). Along with the expansion of attoscience from early investigations of atomic gases to more complex systems [21,25], such as molecules [26], nanoparticles [27,28], and solids [21,24,25,29], the efficient generation of ultrashort pulses of light in solids holds promise to promote the development of table-top intense high-frequency laser sources [16,23,30] and integrated on-chirp digital electro-optical information processing at optical clock speeds [31].

An appealing option for increasing the HHG efficiency is the use of multicolor driving pulses and the optimization of the amplitudes and phases of their spectral constituents, in order to maximize HH yields in specific spectral domains. The spectral sensitivity of the HH yield to the spectral composition of the driving laser pulse was addressed in experimental [20,32–36] and theoretical [30,37–43] studies with atomic [32,37,38,40], molecular [41], and solid targets [20,30,33–36,39,42,43]. Tunable two-color laser fields were also employed in investigations of the dissociation asymmetry of diatomic molecules [44–47] and photoelectron spectra [48,49].

The known sensitivity of HHG to the spectral composition of the driving pulses has recently been examined theoretically for solid targets exposed to two- or three-color laser pulses [39,42]. In these investigations the distinctly different role of the driver electric field and corresponding vector potential is exploited and serves as a guide for both maximizing the HH yield and understanding the intensity-dependent structure of solid HH spectra. For the assumed electronic structure of the investigated direct-band-gap materials, the local band gap between the valence and lowest conduction band is smallest at the center of the first Brillouin zone (BZ) of the solid and increases as crystal momenta shift towards the edge of the BZ (Fig. 1). Conversely, the smallest and largest local band gaps between the lowest and next higher, second conduction band occur at the BZ edge and the Γ point (which designates the center of the first BZ), respectively. The length of the subinterval of crystal momenta within the first BZ, which a valence electron with a given initial crystal momentum can reach within an optical cycle of the driving pulse, is determined by the amplitude of the driving pulse vector potential. This follows from the minimal coupling of the driver vector potential to the crystal momentum. For example, a valence electron starting at the Γ-point requires a sufficiently strong field-induced momentum change to reach a BZ edge. This momentum change being proportional to the driving pulse vector

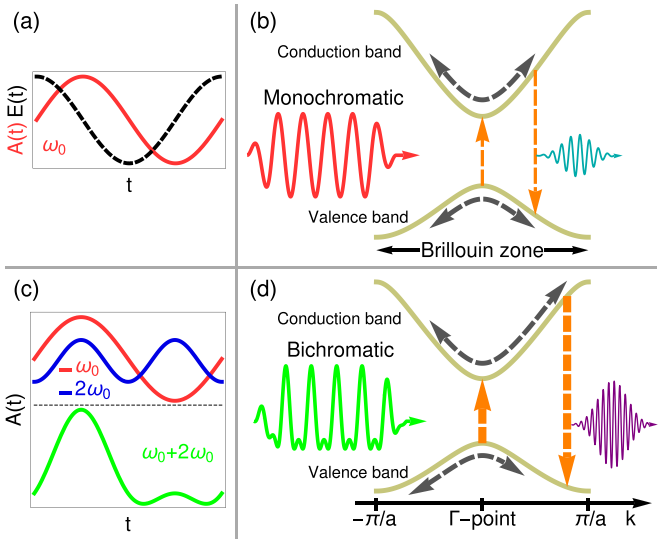

FIG. 1. Mechanisms for HHG in solids by (a), (b) monochromatic and (c), (d) bichromatic pulses. (a) Vector potential $A(t)$ (solid red line) and electric field $E(t)$ (dashed black line) of a monochromatic driving laser pulse with carrier frequency ω_0 over one period $T_{\omega_0} = 2\pi/\omega_0$. (b) Schematic of HHG by a monochromatic driving pulse (red line) interacting with a two-band model solid represented by the dispersion curves of its valence and conduction bands as a function of the crystal momentum k in the first BZ. The induced intraband motion in both bands is indicated as dashed gray arrows. Laser-driven interband excitation and recombination are represented as orange arrows. Electronic intraband and interband currents contribute to the emission of HH radiation (cyan line). (c) Vector potentials for one period of a fundamental (red line) and phase-coherent harmonic pulse (blue line) with frequencies ω_0 and $2\omega_0$, and their superposition into a bichromatic pulse (green line) with harmonic-conversion ratio $R = 0.5$ and chromatic delay $\tau = T_{\omega_0}/8$. (d) Schematic of HHG in a bichromatic driving pulse (green line). The asymmetry and nonsinusoidal shape of the driving pulse modify intraband and interband currents, as compared to a monochromatic driver of identical pulse energy. This changes the HHG spectrum (purple line) and can increase the HHG yield and cutoff frequency.

potential, a minimum value of the vector-potential amplitude is required for a Γ-point electron (with zero initial crystal momentum) to reach a BZ edge. Similar considerations apply to all initial crystal momenta in the first BZ [15].

Thus, ideally, the most efficient interband excitation in direct-band-gap materials requires the best possible compromise between driving a large fraction of electrons close to the minimum band gap, by momentum transfers mediated through coupling to the laser vector potential, and, simultaneously, the presence of a strong instantaneous driving electric field guaranteeing a large tunneling excitation rate [17,42]. The adjustment of the driving vector-potential and electric-field spectral amplitudes and spectral phases thus appears as a promising scheme for optimizing interband HHG yields.

Consistent with this idea of distinguishing the effects of the driving pulse vector potential and electric field, by numerically solving the time-dependent Schrödinger equation (TDSE) for a one-dimensional model solid and by adjusting the spectral amplitudes and phases of $\omega_0 + 3\omega_0$ two-color driving laser pulses, Li *et al.* [39] found a two to three orders of magnitude intensity enhancement in the second plateau regime of their HH spectra, relative to a monochromatic driving field with the same fundamental frequency ω_0 and peak electric field. The authors interpret this HHG enhancement as due to a dominant transition pathway, where valence electrons are first promoted at the Γ point to the first (lowest) conduction band and subsequently driven towards the BZ edge where, in an appropriately shaped pulse, they get efficiently excited across the narrow local band gap to the second conduction band, enabling interband HH emission in the second plateau spectral range. Based on their model calculations, the authors point to possible practical implications of this large enhancement for the generation of HHs from solids at peak electric-field strengths below the damage threshold. Similarly, for intensities below the threshold for excitation of higher conduction bands in ZnO crystals, the two-band calculations of Song *et al.* [42] for $\omega_0 + 3\omega_0$ two-color and $\omega_0 + 3\omega_0 + 5\omega_0$ three-color pulses predict an intensity enhancement in the (first) plateau spectral domain of about two and three orders of magnitude, respectively, relative to a monochromatic driving pulse with the fundamental frequency and same intensity as the fundamental spectral component of the multi-color pulses. As for the work of Li *et al.* [39], the numerically predicted HHG enhancement in appropriately tuned multicolor pulses can be understood as the result of electronic "preacceleration" by the driving pulse vector potential toward the minimal band gap in the BZ (in this case between the valence and conduction bands, at the Γ point), where a strong electric field efficiently excites the active electron. Within a time-frequency analysis, Song *et al.* confirm the importance of preaccelerating valence-band electrons for allowing a large range of initial crystal momenta to contribute to interband HHG.

From a purely theoretical point of view, the preceding discussion may suggest the use of a large number of harmonics for synthesizing driving pulses with a high flexibility for tuning HHG spectra. However, in practice the frequency upconversion to the third- or higher-order odd harmonics is significantly less efficient than second-harmonic generation [50]. For this reason, we limit our study to bichromatic pulses that we envision as being provided by frequency doubling (without loss) an adjustable fraction R of a primary pulse with carrier frequency ω_0 and energy $U_{\omega_0}^{\rm prim}$ [Figs. 1(c) and 1(d)]. The resulting linearly polarized two-color pulse consists of a fundamental pulse of energy U_{ω_0} and a copropagating phase-coherent second-harmonic pulse of energy $U_{2\omega_0}$. We further assume that the centers of the two monochromatic constituents have a controllable delay τ. Such pulses are conveniently produced in the laboratory and have been used, e.g., in molecular dissociation [44] and solid HHG [34] experiments.

In the numerical simulations discussed below, we analyze the yields in different domains of the HH spectrum as functions of the energy-conversion parameter $R = U_{2\omega_0}/U_{\omega_0}^{\rm prim}$ and chromatic delay τ for fixed primary pulse energies $U_{\omega_0}^{\rm prim}$. We perform these reduced-dimensionality calculations for parametrized model crystals and adjust the crystal parameters to reproduce the lowest band gap of MgO crystals. While our model includes electronic excitation to and recombination processes from higher conduction bands, we focus on

optimizing the HH yield in the first plateau region of the HH spectrum by variation of the pulse temporal profile, i.e., of R and τ. HH yields in the second and higher plateau domains are successively orders of magnitude smaller [15,19,51] and thus, to date, not attractive for practical applications [21,25].

We organized this paper as follows. In Sec. II we outline our theoretical framework, starting in Sec. II A with a description of the bichromatic driving laser field used in our calculations. In Sec. II B we review our theoretical scheme for numerically solving the TDSE by expanding the active electron's wave function in a basis of adiabatically field-dressed Bloch states. We continue in Sec. II C with an overview of the proposed HHG mechanism for monochromatic and bichromatic pulses, before discussing our numerical results in Sec. III. In Sec. III A, we discuss the limiting cases of HHG in monochromatic pulses of frequencies ω_0 and $2\omega_0$. Subsequently, in Sec. III B, we compare HHG spectra for bichromatic pulses with two fixed conversion ratios $R = 0.2$ and 0.5, and two chromatic delays $\tau = 0$ and $\pi/(4\omega_0)$. Section III C contains a discussion of field-driven electron trajectories for the specific pulse-shape parameters $R = 0.5$ and $\tau = 0$. In Sec. III D we analyze the integrated below-band-gap and (first) plateau yields for $\tau = 0, \pi/(4\omega_0)$ as functions of R. Following a brief summary and our conclusions in Sec. IV, this work includes three appendices. In Appendix A we formulate how the constraint of a constant primary pulse energy interrelates the pulse shape and electric field amplitudes of a bichromatic pulse. In Appendix B we adapt a semiclassical saddle-point method to derive an approximate analytical expression for the interband HH yield. Finally, in Appendix C, we extend this semiclassical analysis to investigate the oscillatory dependence on R of the integrated plateau HH yields. Unless specified otherwise, we use atomic units ($q_e = m_e = \hbar = 1$) throughout this work.

II. THEORY

A. Bichromatic driving electric field

For our numerical simulations in Sec. III below, we assume HHG by bichromatic driving electromagnetic fields

$$E(t) = E_{\omega_0}(t) + E_{2\omega_0}(t), \tag{1}$$

which are composed as the superposition of two co-propagating pulses $E_{\omega_0}(t)$ and $E_{2\omega_0}(t)$ with carrier frequencies ω_0 and $2\omega_0$. We will refer to these two components as "fundamental" and "harmonic," respectively. We model the profiles of the fundamental and harmonic pulse

$$E_i(t) = E_{0,i} f(t - t_i)\cos\left[n_i\omega_0(t - t_i)\right], \tag{2}$$

with the same "flat-top" electric-field envelope

$$f(t) = \begin{cases} \frac{t}{2T_{\omega_0}} + \frac{\tan(n_i\omega_0 t)}{4\pi n_i}, & 0 \leqslant t \leqslant 2T_{\omega_0} \\ 1, & 2T_{\omega_0} \leqslant t \leqslant 8T_{\omega_0} \\ \frac{10T_{\omega_0} - t}{2T_{\omega_0}} - \frac{\tan(n_i\omega_0 t)}{4\pi n_i}, & 8T_{\omega_0} \leqslant t \leqslant 10T_{\omega_0} \end{cases} \tag{3}$$

where $i = \omega_0,\ 2\omega_0$. The integers $n_{\omega_0} = 1$ and $n_{2\omega_0} = 2$ refer to the fundamental and harmonic frequency, respectively. $E_{0,n_i\omega_0}$ and $t_{n_i\omega_0}$ are the amplitudes and reference times of the two monochromatic pulses, respectively. $T_{\omega_0} = 2\pi/\omega_0$ is the period at the fundamental frequency ω_0. The assumed functional form of the fundamental and harmonic pulse envelope implies equal pulse lengths and a harmonic pulse with twice as many cycles as the fundamental pulse. Without loss of generality, we set $t_{\omega_0} = 0$ and define the adjustable temporal delay between $E_{\omega_0}(t)$ and $E_{2\omega_0}(t)$ in Eq. (1) as $\tau = t_{2\omega_0} - t_{\omega_0} = t_{2\omega_0}$.

The vector potential corresponding to the bichromatic field (1),

$$A(t) = A_{\omega_0}(t) + A_{2\omega_0}(t), \tag{4}$$

consists of monochromatic contributions with amplitudes $A_{0,i}$,

$$\begin{aligned} A_i(t) &= -\int_0^t dt' E_i(t') \\ &= -g(t - t_i)A_{0,i}\sin\left[n_i\omega_0(t - t_i)\right], \end{aligned} \tag{5}$$

and envelopes

$$g(t) = \begin{cases} t/(2T_{\omega_0}), & 0 \leqslant t \leqslant 2T_{\omega_0} \\ 1, & 2T_{\omega_0} \leqslant t \leqslant 8T_{\omega_0} \\ (10T_{\omega_0} - t)/(2T_{\omega_0}), & 8T_{\omega_0} \leqslant t \leqslant 10T_{\omega_0}. \end{cases} \tag{6}$$

Since we assume the two-color pulse to be generated by frequency doubling in a nonlinear medium, energy conservation imposes the incident primary pulse energy $U_{\omega_0}^{\text{prim}}$ to be equal to the sum of the fundamental and harmonic pulse energies after the frequency upconversion U_{ω_0} and $U_{2\omega_0}$, respectively. Thus, the fraction $R = U_{2\omega_0}/U_{\omega_0}^{\text{prim}} \in [0, 1]$ of the primary incident pulse energy is frequency doubled. In our numerical applications in Sec. III, we allow the controlled alteration of the bichromatic pulse shape by variation of the conversion fraction R and chromatic delay τ on the stipulation that the bichromaic pulse energy $U_{\omega_0}^{\text{prim}} = U_{\omega_0} + U_{2\omega_0}$ is kept constant. For the pulse profiles defined in Eqs. (2) and (3), the requirement of a fixed bichromatic pulse energy relates the electric-field and vector-potential amplitudes of the fundamental and harmonic pulse to the field and vector-potential amplitude of the primary incident pulse $E_0 = E_{0,\omega_0}(R = 0)$ and $A_0 = A_{0,\omega_0}(R = 0)$, respectively, as

$$\begin{aligned} E_{0,\omega_0}(R, \tau) &= E_0\left(\sqrt{(1 - R) + \frac{\beta(\tau)^2 R}{\alpha_{\omega_0}\alpha_{2\omega_0}}} - \sqrt{\frac{\beta(\tau)^2 R}{\alpha_{\omega_0}\alpha_{2\omega_0}}}\right), \\ A_{0,\omega_0}(R, \tau) &= A_0\left(\sqrt{(1 - R) + \frac{\beta(\tau)^2 R}{\alpha_{\omega_0}\alpha_{2\omega_0}}} - \sqrt{\frac{\beta(\tau)^2 R}{\alpha_{\omega_0}\alpha_{2\omega_0}}}\right), \end{aligned} \tag{7}$$

and

$$E_{0,2\omega_0}(R) = E_0\sqrt{\frac{\alpha_{\omega_0}}{\alpha_{2\omega_0}}R}, \quad A_{0,2\omega_0}(R) = \frac{A_0}{2}\sqrt{\frac{\alpha_{\omega_0}}{\alpha_{2\omega_0}}R}\,, \tag{8}$$

where $A_0 = E_0/\omega_0$ (cf. Appendix A). The coefficients α and β are defined in Eqs. (A3) and (A5), respectively, and satisfy

$$\sqrt{\frac{\alpha_{\omega_0}}{\alpha_{2\omega_0}}} = 1.0006, \quad \frac{\beta(\tau)^2}{\alpha_{\omega_0}\alpha_{2\omega_0}} < 0.000\,06. \tag{9}$$

In the monochromatic limits $R = 0$ and 1, the pulse amplitudes become independent of τ. In particular, in the absence of the harmonic pulse ($R = 0$), the amplitude relations [Eq. (7)]

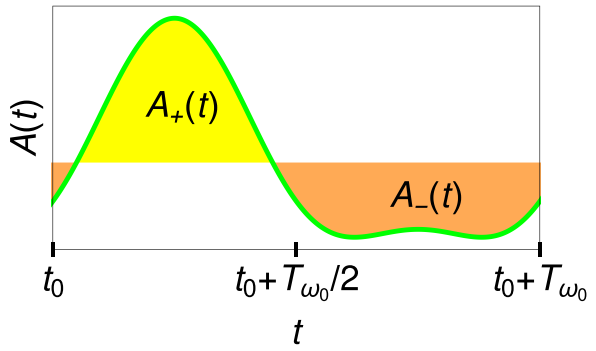

FIG. 2. Definition of the pulse asymmetry parameter $\mathcal{A}$ in Eq. (13) for the flat-top part (i.e., for $t_0 \in [2T_{\omega_0}, 7T_{\omega_0}]$) of a bichromatic pulse with energy-conversion ratio $R = 0.5$ and chromatic delay $\tau = T_{\omega_0}/8$. $A_+(t)$ and $A_-(t)$ represent positive and negative values of the vector potential $A(t)$.

simplify to

$$\begin{aligned} E_{0,\omega_0}(0) &= E_0, \quad E_{0,2\omega_0}(0) = 0, \\ A_{0,\omega_0}(0) &= A_0, \quad A_{0,2\omega_0}(0) = 0\,. \end{aligned} \tag{10}$$

Similarly, for the limiting case of complete harmonic conversion ($R = 1$), we obtain

$$\begin{aligned} E_{0,\omega_0}(1) &= 0, \quad E_{0,2\omega_0}(1) = E_0\sqrt{\frac{\alpha_{\omega_0}}{\alpha_{2\omega_0}}} \approx E_0, \\ A_{0,\omega_0}(1) &= 0, \quad A_{0,2\omega_0}(1) = \frac{A_0}{2}\sqrt{\frac{\alpha_{\omega_0}}{\alpha_{2\omega_0}}} \approx \frac{A_0}{2}. \end{aligned} \tag{11}$$

In the continuous wave (cw) limit, i.e., after replacing the envelope function (3) by $f(t) = 1$, we find $\beta = 0$ and $\alpha_{\omega_0} = \alpha_{2\omega_0}$, and thus the τ-independent amplitude relations

$$\begin{aligned} E_{0,\omega_0}(R) &= E_0\sqrt{1-R}, \quad E_{0,2\omega_0}(R) = E_0\sqrt{R}, \\ A_{0,\omega_0}(R) &= A_0\sqrt{1-R}, \quad A_{0,2\omega_0}(R) = \frac{A_0}{2}\sqrt{R}. \end{aligned} \tag{12}$$

For cw pulses, the monochromatic limits $R = 0, 1$ are thus related as $E_{1,2\omega_0}(0) = E_{0,\omega_0}(0)$ and $A_{0,2\omega_0}(1) = 0.5A_{0,\omega_0}(0)$.

The parameters R and τ determine the shape of the bichromatic pulse, which we quantify by introducing the asymmetry parameter

$$\mathcal{A} = \frac{\int_{t_0}^{t_0+T_{\omega_0}} dt[A_+^2(t) - A_-^2(t)]}{\int_{t_0}^{t_0+T_{\omega_0}} dt[A_+^2(t) + A_-^2(t)]}. \tag{13}$$

This parameter accounts for the different functional forms of the positive $A_+(t) = \Theta[A(t)]A(t)$ and negative pulse segments $A_-(t) = -\Theta[-A(t)]A(t)$, respectively, within one optical cycle T_{ω_0} of the flat part of the pulse profile (3) [$t_0 \in (2T_{\omega_0}, 7T_{\omega_0})$], as illustrated in Fig. 2. Θ designates the Heaviside unit step function.

To better expose the dependence of the HHG spectrum on the shape of the bichromatic driving pulse, we normalize its vector potential and electric field to the primary pulse amplitudes E_0 and A_0:

$$\tilde{E}(t) = \frac{E(t)}{E_0}, \quad \tilde{A}(t) = \frac{A(t)}{A_0}. \tag{14}$$

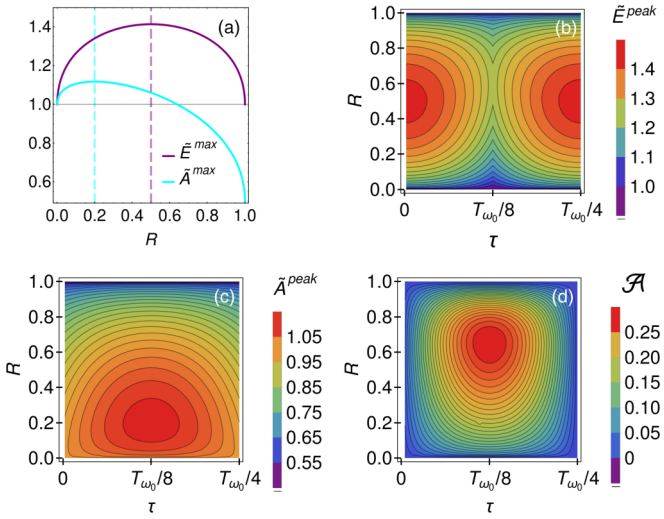

FIG. 3. Characterization of the bichromatic driving field as a function of the harmonic energy-conversion parameter R and chromatic delay τ, in the flat-top part of the pulse profile (3) (i.e., for $t_0 \in [2T_{\omega_0}, 7T_{\omega_0}]$). (a) Maximal field strength and vector potential for all delays τ as a function of R, normalized to the fixed field strength and vector-potential amplitudes of the primary laser according to Eq. (14). Normalized peak values of the (b) electric field and (c) vector potential as functions of R and τ. (d) Pulse asymmetry parameter according to Eq. (13).

Furthermore, for each set of parameters R and τ, we define the peak values of the normalized bichromatic field magnitudes

$$\begin{aligned} \tilde{E}^{\text{peak}}(R,\tau) &= \max_{\forall t} |\tilde{E}(t)|, \\ \tilde{A}^{\text{peak}}(R,\tau) &= \max_{\forall t} |\tilde{A}(t)|, \end{aligned} \tag{15}$$

and their maxima over all delays τ as a function of R,

$$\begin{aligned} \tilde{E}^{\max}(R) &= \max_{\forall \tau} \tilde{E}^{\text{peak}}(R,\tau), \\ \tilde{A}^{\max}(R) &= \max_{\forall \tau} \tilde{A}^{\text{peak}}(R,\tau). \end{aligned} \tag{16}$$

Figure 3(a) shows $\tilde{E}^{\max}(R)$ and $\tilde{A}^{\max}(R)$ as a function of the conversion parameter R. The electric field and vector potential depend differently on the conversion ratio R and reach their maxima at different values $R \in (0, 1)$. Their maximal values $\tilde{E}^{\max}(\frac{1}{2}) = \sqrt{2}$ and $\tilde{A}^{\max}(\frac{1}{5}) = \sqrt{5}/2$ exceed the maximum amplitudes of the monochromatic pulses with frequencies ω_0 and $2\omega_0$ at $R = 0$ and 1, respectively. Since for monochromatic pulses HHG in solids depends crucially on the peak intensity of the driving field [11,12], for bichromatic driving pulses the strong dependence of $\tilde{E}^{\max}(R)$ and $\tilde{A}^{\max}(R)$ on R lets us expect a significant influence of R on HH spectra. This expectation is confirmed by our numerical applications in Sec. III below. As functions of R and τ the normalized peak values $\tilde{E}^{\text{peak}}(R,\ \tau)$ and $\tilde{A}^{\text{peak}}(R,\ \tau)$ reach their maxima at $R = \frac{1}{2}$ and $\tau = 0$ [Fig. 3(b)] and $R = \frac{1}{5}$ and $\tau = T_{\omega_0}/8$ [Fig. 3(c)], respectively. The dependence of the pulse asymmetry (13) on R and τ is shown in Fig. 3(d). The pulse asymmetry obviously vanishes at $\tau = 0$ and is largest along the line $\tau = T_{\omega_0}/8$ at $R \approx \frac{2}{3}$.

B. Solution of the TDSE by expansion in Houston states

For our numerical simulation of bichromatically driven HHG in solids, we adopt the reduced-dimensionality single active electron model we applied to monochromatic driving fields in Ref. [15]. Details of the numerical model can be found in this reference, and we here only present a brief outline of its adaptation to solving the TDSE,

$$\left[\frac{1}{2}[\hat{p}+A(t)]^2+V(x)\right]|\psi(t)\rangle = i\frac{\partial}{\partial t}|\psi(t)\rangle, \tag{17}$$

for the interaction of a single active electron of a one-dimensional infinitely extended solid with the bichromatic 10-cycle flat-top driving laser field $E(t)=-\partial A(t)/\partial t$ defined in the previous section. $\hat{p}=-i\partial/\partial x$ denotes the momentum operator. We represent the solid by a periodic Kronig-Penney potential $V(x)=V(x+a)$ [52,53] with lattice constant a and the dispersion relation between crystal momenta k and energies ε_{nk} in the valence ($n=v$) and conduction bands ($n=c$)

$$\cos(ak)=\cos(a\sqrt{2\varepsilon_{nk}})+\frac{V_0}{\sqrt{2\varepsilon_{nk}}}\sin(a\sqrt{2\varepsilon_{nk}}). \tag{18}$$

We adjust the potential strength V_0 to match the band widths and band gap of the electronic band structure of the solid.

We expand the solutions of Eq. (17),

$$|\psi_k(t)\rangle = e^{-iA(t)x}\sum_n B_{nk}(t)e^{\left[-i\int_0^t dt'\varepsilon_{n\kappa(t')}\right]}|\phi_{n\kappa(t)}\rangle, \tag{19}$$

in a basis of Houston states $|\phi_{n\kappa(t)}\rangle$, which are adiabatic in the field-dressed time-dependent crystal momentum $\kappa(t)=k+A(t)$ and solutions of the Schrödinger equation [12,15]

$$\left[\frac{\hat{p}^2}{2}+V(x)\right]|\phi_{n\kappa(t)}\rangle = \varepsilon_{n\kappa(t)}|\phi_{n\kappa(t)}\rangle. \tag{20}$$

Inserting (19) in (17) results in the set of coupled equations

$$i\dot{B}_{nk}(t) = -E(t)\sum_{n'\neq n}B_{n'k}(t)D^{nn'}_{\kappa(t)}\exp\left[i\int_0^t dt'\Delta\varepsilon^{nn'}_{\kappa(t)}dt'\right], \tag{21}$$

where $\Delta\varepsilon^{nn'}_{\kappa(t)}=\varepsilon_{n\kappa(t)}-\varepsilon_{n'\kappa(t)}$ defines the crystal-momentum-resolved ("local") band-gap energy and

$$D^{nn'}_{\kappa(t)} = \frac{i\int_0^a dx\,\phi^*_{n\kappa(t)}(x)\hat{p}\phi_{n'\kappa(t)}(x)}{a\Delta\varepsilon^{nn'}_{\kappa(t)}} = \frac{i\,P^{nn'}_{\kappa(t)}}{\Delta\varepsilon^{nn'}_{\kappa(t)}} \tag{22}$$

are transition dipole moments, expressed in terms of the momentum-operator matrix elements $P^{nn'}_{\kappa(t)}$ for $n\neq n'$.

Each initial crystal momentum k defines an electronic current

$$J_k(t)=J^{ra}_k(t)+J^{er}_k(t),$$

which consists of intraband and interband contributions

$$J^{ra}_k(t) = -\sum_n \rho^{nn}_k(t)\,P^{nn}_{\kappa(t)}, \tag{23}$$

$$J^{er}_k(t) = -\sum_{n'>n}\sum_n e^{i\int_0^t dt'\Delta\varepsilon^{nn'}_{\kappa(t')}}\rho^{n'n}_k(t)P^{nn'}_{\kappa(t)}+\text{c.c.}, \tag{24}$$

respectively, where $\rho^{nn'}_k(t)=B^*_{nk}(t)B_{n'k}(t)$. Fourier transformation provides the spectral HHG yield from a given k channel

$$Y_k(\omega) = \left|\int_{-\infty}^{\infty}dt\,e^{-i\omega t}J_k(t)\right|^2 \equiv |\hat{J}_k(\omega)|^2 = Y^{ra}_k(\omega)+Y^{er}_k(\omega)+2\hat{J}^{er}_k(\omega)\hat{J}^{ra}_k(\omega), \tag{25}$$

which, in addition to the intraband $[Y^{ra}_k(\omega)]$ and interband $[Y^{er}_k(\omega)]$ yields, includes the interference term $2\hat{J}^{er}_k(\omega)\hat{J}^{ra}_k(\omega)$. Integration over the first BZ results in the total HHG yield

$$Y(\omega) = \left|\int_{-\infty}^{\infty}dt\,e^{-i\omega t}\int_{\text{BZ}}dk\,J_k(t)\right|^2. \tag{26}$$

Corresponding expressions give the total intraband and interband HHG yields $Y^{ra}(\omega)$ and $Y^{er}(\omega)$, respectively.

C. HHG mechanism for bichromatic pulses

Figure 1 compares mechanisms for HHG in a generic two-band solid by monochromatic and bichromatic driving pulses, indicating contributions to the laser-driven intraband currents (23) from both bands and interband currents (24) that arise in response to the laser-induced dipole couplings (22). While both currents contribute to the HH yield, as expressed in Eqs. (25) and (26), the interband current primarily contributes to the spectral range above the minimum band-gap energy $\Delta\varepsilon^{cv}_0$ [15]. For the generic direct band-gap solid assumed in Figs. 1(b) and 1(d), the minimum band gap between the valence and conduction bands occurs at the Γ point. The interband current requires optical excitation out of the valence band, which occurs if

$$\Delta\varepsilon^{cv}_{\kappa(t)}\approx\Delta\varepsilon^{cv}_0, \quad \kappa(t)\approx 0,$$

and leads to harmonic emission due to electron-hole recombination from mainly the lowest conduction band to the valence band. Much smaller contributions to the HH yield are due to recombination from higher conduction bands to the valence band, at significantly higher harmonic energies, and interband transitions between conduction bands [12,15].

The expansion (19) of the light-induced electronic dynamics in terms of Houston states relates intraband and interband currents to the adiabatic exchange of momentum $A(t)$ between the driving field and active electron. The minimal coupling of the field momentum $A(t)$ and the electron's crystal momentum k to the field-dressed crystal momentum $\kappa(t)=k+A(t)$ allows the continuous momentum exchange of the active electron with the external laser field and accelerates the active electron to an anharmonic oscillatory motion. The harmonic composition of this forced anharmonic periodic motion explains the discrete nature of intraband HHG. The propensity of intraband emission to occur at harmonic photon energies below the minimum band-gap energy is consistent with the opening of competing interband excitation channels for higher

spectral components of the photoelectron wave packet. Interband HH emission with photon energies above the minimal band-gap energy $\Delta\varepsilon_0^{cv}$ requires recombination at higher crystal momenta, away from the immediate vicinity of the Γ point, near which electronic dispersion in the solid can be approximated as linear. This explains the field-strength dependence of the cutoff for monochromatic laser sources [17].

In numerical simulations for sufficiently intense monochromatic driving pulses, we traced relevant contributions to the interband HH yield to initial crystal momenta (k channels) in the entire first BZ, yet found interband excitation to occur most likely for field-dressed crystal momenta $\kappa(t) \approx 0$ [15], i.e., close to the Γ point. Within the adiabatic Houston state expansion (19), interband emission can thus be interpreted as a four-step process [54] involving (i) an initial preacceleration of the active electron, driven by the field $A(t)$ resulting in field-dressed momenta $\kappa(t)$, (ii) interband excitation with an intensity proportional to the electric field $E(t)$, (iii) the continued field-driven change of the crystal momenta in the conduction band, and (iv) interband recombination at the instantaneous band-gap energy, as indicated in Figs. 1(b) and 1(d). Qualitatively, this more elaborate sequential scheme can be expected to result in a more subtle anharmonically driven electronic current (24) with more prominent HH-frequency components above the minimal band gap than the intra-valence-band current (23).

This interpretation of intraband and interband harmonic emission emphasizes the distinct importance of the bichromatic vector potential $A(t)$, electric field $E(t)$, and pulse profile in shaping the HH spectrum. In particular, the pulse asymmetry $\mathcal{A}$ is expected to affect the occurrence of even harmonic emission, while the detailed temporal shape of the driving pulse is imprinted on the electron currents (23) and (24), and thus on the HH spectrum (26). As the temporal profiles of the bichromatic vector potentials in Figs. 1(c), 1(d), and 2 illustrate, the chance for an active electron starting in a given k channel in the valence band to be excited to the lowest conduction band near the Γ point is unbalanced for positive and negative values of k, in contrast to HHG with monochromatic driving pulses. Interband emission thus involves both an anharmonic momentum transfer $A(t)$ and an unbalanced effective shift within the first BZ to field-dressed crystal momenta $\kappa(t)$ near the Γ point, where interband excitation is most likely to occur, while the second effect is absent in intra-valence-band HHG. We therefore expect interband HH emission to depend differently on the temporal profile of the bichromatic driving pulse than intraband HHG.

While the simple interpretation and qualitative reasoning presented in this section cannot explain all features of measured and numerically simulated HH spectra, the specific numerical examples discussed in Sec. III below confirm the suggested propensities. Without resorting to the fully quantum-mechanical numerical simulation results presented in Sec. III, some key features of HHG in solids can be revealed based on a semiclassical saddle-point approximation to the quantum-mechanically calculated current [Eq. (24)] [13,15]. For monochromatic driving fields, this approximation predicts contributions from initial crystal momenta k to depend exponentially on the square root of the reduced effective electron-hole-pair mass at the Γ point m_0^* (defined in Appendix B), minimal band-gap energy $\Delta\varepsilon_0^{cv}$, and inverse electric-field strength of the primary pulse E_0:

$$Y_k^{er} \propto \exp\left[-\frac{\sqrt{8m_0^*}\left(\Delta\varepsilon_0^{cv}\right)^{3/2}}{E_0\sqrt{1-(k/A_0)^2}}\right]. \tag{27}$$

This results in the approximate BZ-integrated interband yield [15] being proportional to

$$Y^{er}(\omega) \propto \exp\left[-\frac{\sqrt{8m_0^*}\left(\Delta\varepsilon_0^{cv}\right)^{3/2}}{E_0}\right]. \tag{28}$$

The numerical examples presented in Ref. [15] for monochromatic driving pulses demonstrate that these interband transitions mainly contribute to the plateau region of the HH spectrum. The approximations leading to Eq. (27) restrict contributing crystal momenta to $k \in (-A_0, A_0)$, such that the total HH yield (26) increases with increasing peak electric-field strength due to both, an increased range of contributing k channels (proportional to A_0) and the diminishing magnitude of the negative exponent (proportional to $1/E_0$). Once the driving field strength has increased to the point where A_0 equals half the extent of the first BZ, π/a, all k channels can be excited to the conduction band via the Γ point.

The generalization of the semiclassical formula (27) to HHG by bichromatic driving laser fields is derived in Appendix B as

$$Y_k^{er}(\omega) \propto \exp\left[-\frac{\left(\sqrt{8m_0^*}\Delta\varepsilon_0^{cv}\right)^{3/2}}{E_0\tilde{E}[\tilde{A}^{-1}(-k/A_0)]}\right], \tag{29}$$

where $\tilde{A}^{-1}$ is the inverse function of the normalized bichromatic vector potential $\tilde{A}$, and $\tilde{E}$ is the normalized bichromatic electric field, as defined in Eq. (14). This equation reduces to Eq. (27) for $R = 0$. These contributions to the HH spectrum are restricted to k channels with $k \in (-A_0\tilde{A}^{\text{peak}}, A_0\tilde{A}^{\text{peak}})$. As shown in Appendix B, we can further approximate the BZ-integrated interband yield as

$$Y^{er}(\omega) \propto \exp\left[-\frac{\sqrt{8m_0^*}\left(\Delta\varepsilon_0^{cv}\right)^{3/2}}{E_0\tilde{E}^{\text{peak}}(R,\,\tau)}\right], \tag{30}$$

where E^{peak} is defined in Eq. (15). This equation reduces to Eq. (28) for $R = 0$.

As shown in Figs. 3(a) and 3(b), the peak bichromatic electric field $E^{\text{peak}}(R, \tau)$ for any $R \in (0, 1)$ exceeds that in both monochromatic limits. According to Eq. (30) we therefore expect the HH yield for $R \in (0, 1)$ to be larger than for HHG by either the fundamental or harmonic pulse alone. Furthermore, as displayed in Figs. 3(a) and 3(c), for appropriate harmonic energy-conversion ratios R, the scaled peak vector potential $\tilde{A}^{\text{peak}}(R, \tau)$ can be larger than its monochromatic limits $R = 0$ and 1 of a purely fundamental or purely harmonic driving pulse, respectively. Due to the larger peak vector potential of bichromatic pulses, as compared to monochromatic fundamental and harmonic pulses with the same energy, for peak amplitudes $A_0 < \pi/(2a)$ bichromatic interband HHG accesses a larger range of k channels. This suggests an enhanced HH yield and harmonic cutoff extension for HHG by tailored bichromatic fields with appropriate parameters R and

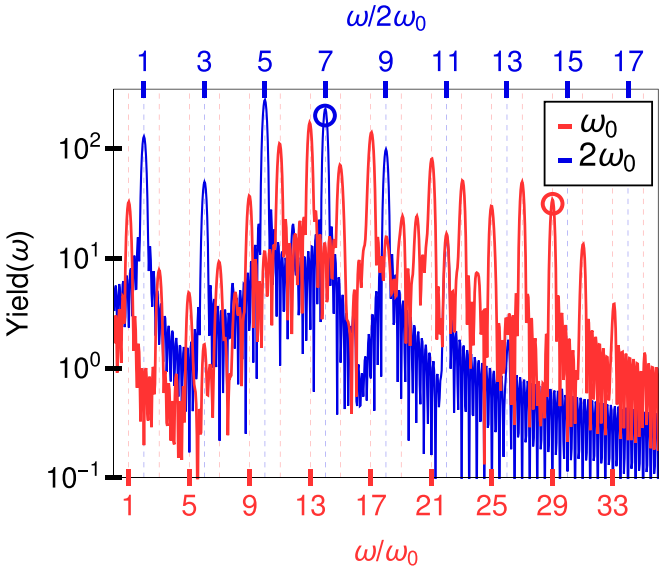

FIG. 4. HHG spectra for a monochromatic flat-top pulse with 10 optical cycles, carrier frequency $\omega_0 = 0.014$ (corresponding to a wavelength of 3200 nm), and peak electric-field strength of 0.15 V/Å (corresponding to a peak intensity of 3.0×10^{11} W/cm^2) (red line). The blue line shows the spectrum generated by a frequency-doubled monochromatic pulse of equal pulse energy, peak electric-field strength, length, and profile. The red and blue circles indicate the assigned cutoff harmonic orders for spectra generated by the ω_0 and $2\omega_0$ pulses, respectively.

τ. Our numerical results in the following Sec. III by and large confirm these expectations (cf. Figs. 7 and 8 below).

We conclude this section by quantitatively comparing the two limiting cases of HHG by either only the monochromatic fundamental pulse of carrier frequency $\omega_0 = 0.014$ (corresponding a wavelength of 3200 nm, limiting case of $R = 0$) or only the harmonic pulse of frequency $2\omega_0$ (limiting case of $R = 1$). According to Eqs. (9)–(11), at equal pulse energy the monochromatic limits $R = 0, 1$ of flat-top pulses with envelopes given by Eqs. (3) or (6) are related by

$$E_{0,2\omega_0}(1) = E_{0,\omega_0}(0)\sqrt{\frac{\alpha_{\omega_0}}{\alpha_{2\omega_0}}} = 1.0006\, E_{0,\omega_0}(0),$$

$$A_{0,2\omega_0}(1) = 0.5\, A_{0,\omega_0}(0)\sqrt{\frac{\alpha_{\omega_0}}{\alpha_{2\omega_0}}} = 0.5003\, A_{0,\omega_0}(0). \quad (31)$$

Frequency doubling thus does not noticeably alter the peak electric-field strength, but reduces the peak vector potential by 50%, as seen in Fig. 3(a). Based on the semiclassical proportionality (28), we thus expect comparable HH interband yields in the plateau region for HHG by the fundamental and harmonic pulse. This expectation is confirmed by our numerical results in Sec. III A (cf. Fig. 4).

III. NUMERICAL RESULTS

In this section we explore the dependence of HHG on the bichromatic pulse form as a function of the harmonic energy-conversion factor R and chromatic delay τ for the fixed power densities of the driving pulse of 1.6×10^{11} and 3.0×10^{11} W/cm^2, corresponding to peak electric-field strengths of $E_0 = 0.11$ and 0.15 V/Å, respectively. For this purpose, we performed numerical calculations based on the quantum-mechanical model described in Sec. II for two-color pulses composed of a fundamental pulse with a carrier frequency of $\omega_0 = 0.014$ (3200 nm) and a phase-coherent harmonic pulse of frequency $2\omega_0 = 0.028$ (1600 nm). The shape of the bichromatic pulse is defined in Eqs. (1)–(3). The constituent harmonic and fundamental pulses have identical pulse lengths and flat-top envelopes.

In our numerical applications, we use a fourth-order Runge-Kutta algorithm to solve Eq. (21) at 400 equally spaced k points in the first BZ to obtain the expansion coefficients $B_{nk}(t)$. To ensure convergence, we included the 13 lowest bands of the Kronig-Penney model MgO crystal in all calculations. The four lowest bands are depicted in Fig. 12 of our previous publication [15].

We adjusted the crystal-potential strength of the Kronig-Penney model potential $V_0 = 22.345$ eV and interlayer spacing $a = 8$ a.u. to the electronic structure calculated for MgO along the Γ-X direction by Xu and Ching [55]. This full-dimensionality density functional theory (DFT) calculation employs an orthogonalized linear combination of atomic orbitals approach in local density approximation (LDA) and yields a minimal band-gap energy between the valence and conduction bands of $\Delta\varepsilon_0^{cv} = 4.19$ eV. We note that LDA calculations tend to underestimate experimental band-gap values. For MgO this difference amounts to 3 eV [56] within the entire BZ. Focusing on the effect of the driver temporal profile on HHG, we here use a rather simple band-structure model, which captures some characteristics of the MgO band structure in the Γ-X direction, in conjunction with the LDA calculated value for $\Delta\varepsilon_0^{cv}$ of Ref. [55]. Obviously, our reduced-dimensionality model is not able to capture all characteristics of the full three-dimensional crystal structure of MgO, such as, e.g., the angular anisotropy of its HH spectrum [57].

Before discussing HH spectra for bichromatic pulses with $0 < R < 1$ in Secs. III B and III D, we examine the limiting cases of HHG by either the fundamental or the harmonic pulse in the following subsection.

A. HHG in the monochromatic limits

Figure 4 shows HH spectra generated by a driving pulse consisting of either only the fundamental or only the second-harmonic color, calculated quantum mechanically as outlined in Sec. II B. As expected for monochromatic driving pulses, both spectra have a negligible yield of even harmonics. The red and blue circles identify the harmonic cutoff frequencies $\omega \approx 29\,\omega_0$ and $\omega \approx 14\,\omega_0$, respectively, for the ω_0 and $2\omega_0$ driving pulses. We define the cutoff frequency for the monochromatic limits as the last harmonic above which the yield drops linearly on a logarithmic scale. As we will see in the next section, this definition is more difficult to apply for bichromatic pulses, and we will introduce a specific criterion for that case. The fact that the cutoff frequency of the spectrum of the harmonic pulse ($14\,\omega_0$) is approximately half of that of the fundamental ($29\,\omega_0$) is expected because the second-harmonic driver has approximately half the vector-potential amplitude of the fundamental. The net harmonic yields in the

plateau region between $\omega \approx 10\,\omega_0$ and the cutoff harmonic frequency of $\approx 29\,\omega_0$ are approximately the same, consistent with the comparable peak electric-field strengths and the semiclassical estimate given by Eq. (28). The frequency-integrated total HH yield produced by the frequency-doubled pulse $\int d\omega\, Y(\omega)$ is 48% smaller than the total yield generated by the fundamental pulse, even though the two driving pulses generate similar plateau intensities. The smaller integrated yield of the frequency-doubled driver pulse is due to the more rapid decrease of its HH yield for frequencies above $\approx 14\,\omega_0$.

B. HHG spectra for two-color pulses with chromatic delays $\tau = 0$ and $T_{\omega_0}/8$

As shown in Figs. 3(b) and 3(c), the peak electric field and vector potential of bichromatic pulses with equal pulse energy are largest for $\tau = 0$ and $T_{\omega_0}/8$, respectively, and for specific (different) values of the conversion ratio R. Chromatic delays of $\tau = 0$ and $T_{\omega_0}/8$ and specific values of $R \in (0, 1)$ maximize either the peak electric field or vector potential of the two-color pulse to values that exceed the respective peak values in the two monochromatic limits ($R = 0, 1$). These specific values of τ are therefore of particular interest for the search of the largest possible HH yields and HH cutoff frequencies.

The HH spectra in Fig. 5 are calculated for a primary pulse with an amplitude of $E_0 = 0.15$ V/Å and either $\tau = 0$ [Figs. 5(a) and 5(c)] or $\tau = T_{\omega_0}/8$ [Figs. 5(b) and 5(d)]. In particular, the spectrum in Fig. 5(a) is obtained at the maximal electric-field strength $E^{\max} = 0.21$ V/Å of bichromatic pulses with parameters $\tau = 0$ and $R = 0.5$, while the spectrum in Fig. 5(d) is computed for bichromatic pulses with maximal vector potential amplitude $A^{\max} = 0.23$ a.u. achieved for $\tau = T_{\omega_0}/8$ and $R = 0.2$ [cf. Figs. 3(b) and 3(c)]. All spectra in Fig. 5 are shown in comparison with HHG by the fundamental pulse alone (i.e., for $R = 0$).

For all graphs in Fig. 5, the bichromatic pulses generate larger total integrated harmonic yields than monochromatic ω_0 driving pulses. The bichromatic pulses generate HHs at even multiples of the fundamental frequency ω_0. Even harmonics appear not only at odd multiples of the harmonic frequency $2\omega_0$ ($n\omega_0$, $n = 2, 6, 10, \ldots$), since the asymmetric profile of the coherent bichromatic pulse breaks the symmetry of the HHG process. For $\tau = T_{\omega_0}/8$, the appearance of even HHs is consistent with our analysis in Appendix B. This analytical study shows that for $0 < R < 1$ maximal contributions to the HH yield arise from k channels with nonzero initial crystal momenta k_0. Thus, for driving pulses with asymmetrical temporal profile, the adiabatic crystal momentum $\kappa(t) = k_0 + A(t)$ does not "explore" the first BZ symmetrically. A similar behavior is expected for all chromatic delays τ for which $\mathcal{A} \neq 0$.

The total integrated yield for the two-color HHG spectrum in Fig. 5(a) is larger than in Fig. 5(b). This is consistent with the larger maximal electric-field strength of the bichromatic driver and particularly relevant for HHG in the plateau spectral domain. The determination of the cutoff frequency for the bichromatically generated spectra in Fig. 5 is more difficult than for monochromatic driving pulses. We tentatively assign almost equal cutoff orders (relative to the fundamental frequency ω_0) for the bichromatic pulses in Figs. 5(a) and 5(b), 27 and 26, respectively. This suggests that the most obvious benefit of maximizing the bichromatic-pulse peak electric field is a significant enhancement of the plateau harmonic yield.

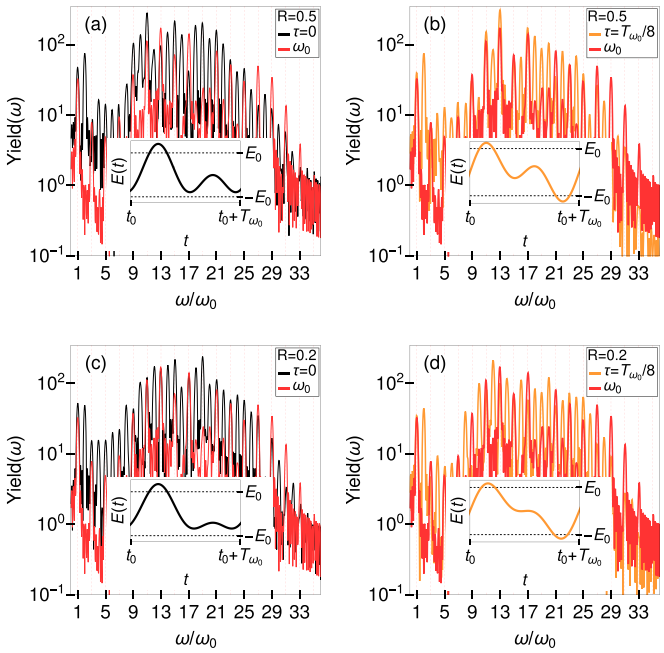

FIG. 5. HH spectra generated by $\omega_0 + 2\omega_0$ bichromatic pulses (black and orange lines) in comparison with spectra generated by the monochromatic primary pulse (red line) with the fundamental frequency ω_0 (corresponding to a wavelength of 3200 nm) of equal pulse energy. The electric-field amplitude of the monochromatic pulse is 0.15 V/Å (corresponding to a peak intensity of 3×10^{11} W/cm^2). The chromatic delays and energy-conversion ratio of the bichromatic pulses are (a) $\tau = 0$, $R = 0.5$ (maximizing the peak bichromatic electric-field strength), (b) $\tau = T_{\omega_0}/8$, $R = 0.5$, (c) $\tau = 0$, $R = 0.2$, and (d) $\tau = T_{\omega_0}/8$, $R = 0.2$ (maximizing the peak bichromatic vector-potential amplitude). The corresponding electric fields over one optical period T_{ω_0} in the flat part of the pulse profile are shown as insets.

The total integrated yield of the two-color HHG spectrum in Fig. 5(c) is larger than in Fig. 5(d), which again is consistent with the larger maximal electric-field strength of the bichromatic driver. On the other hand, even though the peak vector potential is maximal for $R = 0.2$ and $\tau = T_{\omega_0}/8$, we do not see an increase of the cutoff energy. This might be due to the fact that the increase in the peak vector potential of the bichromatic pulse is only 10% larger than for the primary pulse. We will see in the following subsection that the most obvious change in the cutoff frequency occurs for $0.5 < R < 1.0$. In this R interval, the peak vector potential decreases to 50% of its peak value for all R, and the cutoff energy follows closely its variation with R.

The integrated yield obtained for the parameters used in Fig. 5(a) (which maximize the field strength) is greater than that of Fig. 5(d) (obtained for maximal vector potential). This implies that increasing the field strength by manipulating the pulse shape at constant pulse energy is the most efficient way to enhance the harmonic yield. Even though the variation of the vector potential shifts the cutoff frequencies, as we will see

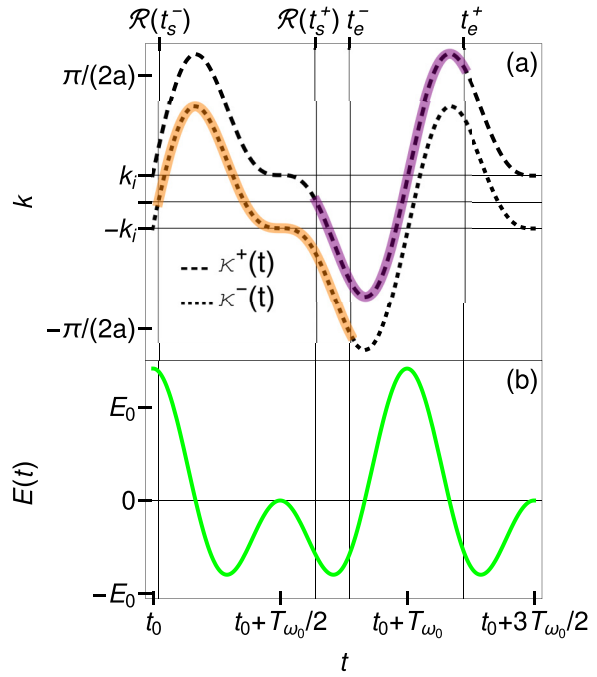

FIG. 6. k-space trajectories for bichromatic laser pulses with energy-conversion ratio $R = 0.5$, chromatic delay $\tau = 0$, and $E_0 = 0.15$ V/Å for $t_0 \in [2T_{\omega_0}, 7T_{\omega_0}]$. (a) Adiabatic momenta $\kappa^+(t) = k_i + A(t)$ (dashed line) and $\kappa^-(t) = -k_i + A(t)$ (dotted line), with $k_i = 0.2A_0$. $\mathrm{Re}(t_s^+)$ and $\mathrm{Re}(t_s^-)$ are tunneling times. t_e^+ and t_e^- are emission times. The purple and orange segments represent semiclassical trajectories $k(t)$ in the $k = k_i$ and $-k_i$ channels, respectively. (b) Probe-laser electric field.

in Sec. III D below, the maximum vector potential achieved by the two-color pulse is not high enough to observe an extension of the cutoff.

C. k-space trajectory analysis for $\tau = 0$

For $\tau = 0$, the maximal contribution to the HH yield is given by the $k = 0$ channel. In this case $\mathcal{A} = 0$, and trajectories with symmetric initial momenta $k = k_i$ and $k = -k_i$ can add complementary contributions to the current that remove even harmonics from the spectrum, as was previously found for monochromatic driving pulses (see Fig. 3 in [15]). For bichromatic pulses, the interplay between the vector potential $A(t)$, which drives electrons along the BZ, and the electric field $E(t)$, which governs the tunneling from the valence to the conduction band at $\kappa(t) \approx 0$ [see Eqs. (B9) and (B11)], is different from the monochromatic case. Thus, even harmonics are expected to be observed for $\tau = 0$ and $0 < R < 1$, as we will show with a specific example.

Figure 6(a) displays the adiabatic crystal momenta $\kappa^+(t) = k_i + A(t)$ and $\kappa^-(t) = -k_i + A(t)$ for $R = 0.5$, $\tau = 0$, $k_i = 0.2A_0$, and $E_0 = 0.15$ V/Å. Figure 6(b) shows the corresponding driver electric field. The tunneling times t_s^+ and t_s^- are determined by Eq. (B4) and depend on the instantaneous field strengths $|E[\mathrm{Re}(t_s^+)]|$ and $|E[\mathrm{Re}(t_s^-)]|$, while the emission times t_e^+ and t_e^- are given by Eq. (C2). $\mathrm{Re}(t_s)$ denotes the real part of t_s. The graph highlights two k-space trajectories with initial crystal momenta $\pm k_i$ that contribute to the BZ-integrated interband yield. For these trajectories, the electric-field strength at the tunneling time is different, $[|E[\mathrm{Re}(t_s^-)]| > |E[\mathrm{Re}(t_s^+)]|]$. This implies that the trajectory which starts at $k = -k_i$ is asymmetrical with respect to the center of the band and will generate even harmonics. These cannot be fully compensated by destructive interference with harmonics from the trajectory starting at $k = k_i$, since the two trajectories are exposed to different electric fields.

D. Integrated HH yields in the below-band-gap and plateau spectral domain

In this section we discuss specific spectral domains $\omega \in [\omega_a, \omega_b]$ for HHG by bichromatic pulses with the chromatic delays assumed in the preceding subsection, $\tau = 0$ and $T_{\omega_0}/8$, and the full range of pulse energy-conversion parameters $R \in [0, 1]$. In particular, we examine the frequency-integrated bichromatic yields $Y_{\omega_0+2\omega_0}(\omega)$, normalized to the HH yield $Y_{\omega_0}(\omega)$ generated in the same domain by a monochromatic pulse with frequency ω_0 of equal energy. For this purpose we define the spectral domain enhancement

$$\bar{Y}(\omega_a, \omega_b) = \frac{\int_{\omega_a}^{\omega_b} d\omega\, Y_{\omega_0+2\omega_0}(\omega)}{\int_{\omega_a}^{\omega_b} d\omega\, Y_{\omega_0}(\omega)} \tag{32}$$

and calculate HH spectra generated by bichromatic pulses at 101 equally spaced spectral ratios $R \in [0, 1]$ for each pulse energy and chromatic delay. By definition, $\bar{Y}(\omega_a, \omega_b) = 1$ for $R = 0$. Furthermore, for a sufficiently large spectral range $[\omega_a, \omega_b]$, $\bar{Y}(\omega_a, \omega_b) < 1$ for $R = 1$ (cf. Fig. 4). In the monochromatic limits ($R = 0, 1$), the parameter τ becomes meaningless and $\bar{Y}(\omega_a, \omega_b)$ independent of τ.

We focus our attention on the spectral-domain enhancement in two spectral ranges, the below-band-gap domain (designated as "<BG") and the plateau region of the HH spectrum. The BG domain is defined by HH photon energies below the minimal band gap of the solid (here 4.2 eV), corresponding approximately to the 10th harmonic of the fundamental frequency. We thus define the BG enhancement as $\bar{Y}_{<\mathrm{BG}} = \bar{Y}(0, 10\,\omega_0)$. The plateau spectral region lies between the minimum band gap and the cutoff frequency $\omega_{0,\mathrm{cut}}$ of the primary pulse, and we define the plateau enhancement according to $\bar{Y}_{\mathrm{plateau}} = \bar{Y}(10\,\omega_0, \omega_{0,\mathrm{cut}})$.

Changes of some relevant characteristics of bichromatic pulses with $\tau = 0$ and $T_{\omega_0}/8$ for $R \in [0, 1]$ are summarized in the top row of graphs in Fig. 7 in terms of the normalized peak electric field $\tilde{E}^{\mathrm{peak}}$ [Fig. 7(a)], normalized peak vector potential $\tilde{A}^{\mathrm{peak}}$ [Fig. 7(b)], and bichromatic pulse asymmetry $\mathcal{A}$ [Fig. 7(c)]. The peak electric field is largest for $\tau = 0$ and the peak vector potential for $\tau = T_{\omega_0}/8$.

Corresponding spectral domain enhancements and cuttoff energies are given in the bottom-row graphs in Fig. 7 as a function of R. For most values of $R \in (0, 1)$ and both considered chromatic delays, the BG in Fig. 7(d) and plateau yields in Fig. 7(e) exceed the monochromatic yields in the same interval of HH frequencies. More specifically, with the exception of a small range of R values near $R = 0.1$ for $\tau = T_{\omega_0}/8$, the considered bichromatic pulses more efficiently generate BG harmonics [Fig. 7(d)]. Similarly, except for conversion ratios $R \gtrsim 0.9$, for both chromatic delays, the

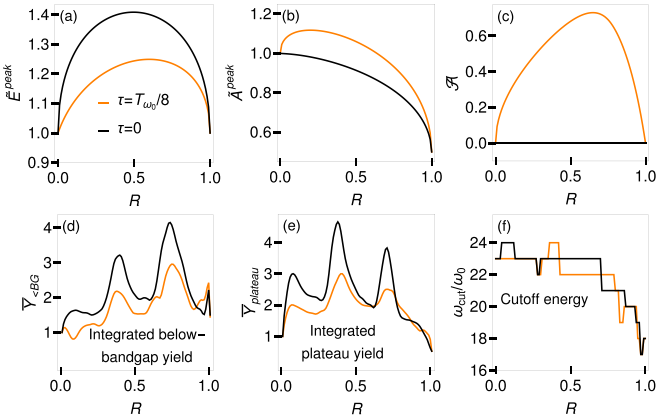

FIG. 7. (a) Peak electric-field strength $\tilde{E}^{\text{peak}}$, (b) peak vector potential $\tilde{A}^{\text{peak}}$, and (c) pulse asymmetry $\mathcal{A}$ of bichromatic driving pulses with chromatic delays $\tau = 0,\ T_{\omega_0}/8$ as functions of the pulse energy-conversion parameter R. $\tilde{E}^{\text{peak}}$ and $\tilde{A}^{\text{peak}}$ are normalized to the maximal electric-field strength $E_0 = 0.11$ V/Å and maximal vector potential $A_0 = 0.15$ a.u., respectively, of a monochromatic pulse with the same pulse energy. Spectral domain enhancements, (d) $\bar{Y}_{<\text{BG}}$ for the below-band-gap, and (e) $\bar{Y}_{\text{plateau}}$ for the plateau spectral range of the HH spectrum. (f) Cutoff harmonic order.

two-color-pulse-produced HH yields clearly exceed the yield of the limiting monochromatic pulses [Fig. 7(e)].

Figures 7(d) and 7(e) show that the integrated BG and plateau yields are larger for $\tau = 0$ than for $\tau = T_{\omega_0}/8$, except for very small intervals of R values near the $R = 1$ ($2\omega_0$ driving pulse) limit. This is consistent with the driving pulse reaching larger electric field strengths for $\tau = 0$. The cutoff energy tends to be largest and close to the monochromatic $R = 0$ (ω_0 driving pulse) limit for $0 < R \lesssim 0.6$. As a function of R it is modulated by peaks and steps that are due to the discrete nature of HHs and the above-mentioned difficulty in clearly assigning HH cutoff frequencies. For $0.5 < R < 1$, the variation of the peak vector potential is approximately 50%, and the cutoff energy follows its functional form for both chromatic delays. While the different peak electric fields for the two considered chromatic delays appear to strongly affect the HH yields, we cannot identify a systematic change in the HH yield due to the larger peak values of the vector potential for $\tau = T_{\omega_0}/8$ in the numerical examples discussed in this work. The bichromatic pulse asymmetry $\mathcal{A}$ in Fig. 7(c) does not provide guidance to spectral domains with enhanced HH yields. For $\tau = 0$, this is obvious since $\mathcal{A} = 0$ [see Fig. 3(d)]. For $\tau = T_{\omega_0}/8$, $\mathcal{A}$ is larger than zero and reaches a maximum at $R = 0.66$ without clearly imposing its functional dependence on R on the HH yields in Fig. 7.

Figure 8 shows integrated normalized yields for the same spectral domains as in Figs. 7(d)–7(f), and cutoff harmonic orders, for a higher driving pulse energy that is equal to the energy of a fundamental pulse of peak field strength $E_0 = 0.15$ V/Å. As for the lower pulse energy in Fig. 7, the integrated BG and plateau yields oscillate in R. At the larger pulse energy in Fig. 8 the relative enhancement in the spectral region above the band gap is smaller. According to Eq. (30) the above-band-gap HH yield depends exponentially on the inverse field strength E_0. It monotonically increases and saturates as E_0

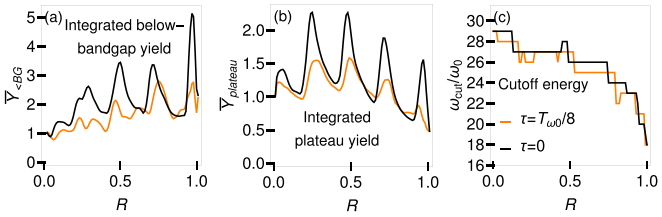

FIG. 8. As Figs. 7(d)–7(f), for a maximal electric-field strength of $E_0 = 0.15$ V/Å.

increases. Thus, under the approximations made in Eq. (30), for increasing E_0, we expect the relative yield enhancement to decrease. This is consistent with the overall behavior of the plateau yields in Fig. 7(e) as compared with Fig. 8(b).

As a function of the second-harmonic energy-conversion parameter R, the normalized HH yields in Figs. 7(d), 7(e), 8(a), and 8(b) show pronounced peaks. The spacing δR between peaks is smaller for the higher pulse energy in Figs. 8(a) and 8(b). For the integrated plateau yields in Figs. 7(e) and 8(b), it amounts to $\delta R(E_0 = 0.11\ \text{V/Å}) \approx 0.33$ and $\delta R(E_0 = 0.15\ \text{V/Å}) \approx 0.23$, respectively. The larger values of δR at the lower pulse energy are in fair agreement with the semiclassical analysis in Appendix C. As derived in Appendix C, δR is approximately inversely proportional to E_0, i.e.,

$$\frac{\delta R(E_0 = 0.15\ \text{V/Å})}{\delta R(E_0 = 0.11\ \text{V/Å})} = \frac{0.11}{0.15} \approx 0.73, \tag{33}$$

in favorable agreement with the ratio extracted from our quantum-mechanically calculated yields in Figs. 7(e) and 8(b) of $0.23/0.33 = 0.70$. Physically, we trace the oscillatory structure of the high harmonic yields in Figs. 7 and 8 to the R-dependent interference of k channels [cf. Eq. (26)].

IV. SUMMARY AND CONCLUSIONS

We theoretically investigated HHG by bichromatic pulses from a crystalline solid in single active-electron approximation, adjusting a one-dimensional Kronig-Penney model potential to the DFT-LDA calculated MgO electronic structure in Ref. [55]. We solve the TDSE by expanding the active electron's wave function in a basis of adiabatically field-dressed Bloch states (Houston states) in order to calculate HH spectra for bichromatic laser pulses with variable (i) chromatic delay between their fundamental and second-harmonic frequency components and (ii) second-harmonic energy-conversion ratio. In all calculations we assumed flat-top temporal pulse profiles extending over 10 optical cycles of the fundamental pulse component and kept the pulse energy fixed while examining the influence of the bichromatic-pulse temporal profile on HH spectra.

Interpreting our numerical results within a semiclassical saddle-point approximation and in relation to the different dependence of the driving laser pulse electric field and vector potential, we assessed the (i) crystal momentum range of k channels, which effectively contributes to HHG in distinct spectral domains and (ii) yield enhancement in the BG and plateau region of the HH spectrum as a function of the driving pulse shape parameters and intensity. Our numerical applications demonstrate that tuning the shape of a bichromatic

driving laser electric fields, by variation of the fundamental versus second-harmonic pulse amplitude ratio and delay under the constraint of a constant pulse energy, can significantly enhance HH yields and modify the HH cutoff frequency.

ACKNOWLEDGMENTS

This work was supported by NSF Grant No. 1802085 and the Air Force Office of Scientific Research under Award No. FA9550-17-1-0369. Any opinions, findings, and conclusions or recommendations expressed in this material are those of the authors and do not necessarily reflect the views of the United States Air Force. U.T. acknowledges partial support from the Chemical Sciences, Geosciences, and Biosciences Division, Office of Basic Energy Sciences, Office of Science, U. S. Department of Energy under Award No. DEFG02-86ER13491.

APPENDIX A: ELECTRIC-FIELD AMPLITUDES

The energy of a linearly polarized homogeneous electric pulse $E(t)$ is given by [58]

$$U_0 = \frac{cD}{4\pi}\int_{-\infty}^{\infty} dt\, E^2(t), \tag{A1}$$

where D is the area of a plane transverse to the propagation direction, c is the velocity of light in vacuum, and the factor $(4\pi)^{-1}$ is the permittivity of vacuum in atomic units.

In particular, the energy of the primary monochromatic pulse with the fundamental carrier frequency ω_0 (i.e., for $R = 0$) is

$$U_{\omega_0}^{\text{prim}} = \frac{cD}{4\pi}E_0^2\int_0^{NT} dt\, f^2(t)\cos^2(\omega_0 t) = \frac{cD}{4\pi}E_0^2\alpha_{\omega_0}, \tag{A2}$$

with the definition

$$\alpha_i = \int_0^{NT} dt\, f^2(t)\cos^2(n_i\omega_0 t), \quad i = \omega_0,\ 2\omega_0. \tag{A3}$$

Accordingly, the energy of a bichromatic pulse with arbitrary values of R and τ, defined in Eqs. (1)–(3), is given by

$$U = \frac{cD}{4\pi}\left[E_{0,\omega_0}^2\alpha_{\omega_0} + 2E_{0,\omega_0}E_{0,2\omega_0}\beta(\tau) + E_{0,2\omega_0}^2\alpha_{2\omega_0}\right], \tag{A4}$$

where

$$\beta(\tau) = \int_0^{NT+\tau} dt\, f(t)f(t-\tau)\cos(\omega_0 t)\cos[2\omega_0(t-\tau)]. \tag{A5}$$

This allows us to write the energy-conversion ratio as

$$R = \frac{U_{2\omega_0}}{U_{\omega_0}^{\text{prim}}} = \frac{E_{0,2\omega_0}^2\alpha_{2\omega_0}}{E_0^2\alpha_{\omega_0}}, \tag{A6}$$

where $U_{2\omega_0} = (cD/4\pi)E_{0,2\omega_0}^2\alpha_{2\omega_0}$ is the energy of the harmonic pulse.

Since we assume the energy of the bichromatic pulses defined by Eqs. (1)–(3) to be independent of the harmonic conversion ratio R and chromatic delay τ, $U_{\omega_0}^{\text{prim}} = U$, and therefore

$$E_{0,\omega_0} = E_0\left(\sqrt{(1-R) + \frac{\beta(\tau)^2 R}{\alpha_{\omega_0}\alpha_{2\omega_0}}} - \sqrt{\frac{\beta(\tau)^2 R}{\alpha_{\omega_0}\alpha_{2\omega_0}}}\right). \tag{A7}$$

APPENDIX B: SADDLE-POINT ANALYSIS OF THE INTERBAND YIELD FOR BICHROMATIC DRIVING PULSES

Following the saddle-point analysis in Ref. [15], we approximate the interband current given by Eq. (36) in [15] as

$$\left|\hat{j}_k^{er}(\omega)\right| \propto \left|\sum_{t_s}\sum_{t_e} j_{k_r}^{er}(t_e, t_s)\right| \leqslant \sum_{t_s}\sum_{t_e}\left|j_k^{er}(t_e, t_s)\right|,$$

where

$$\left|j_k^{er}(t_e, t_s)\right| = \frac{|E(t_s)|e^{\text{Im}[S(k,\,t_e,\,t_s)]}}{|\det[\text{Hess}\,\sigma_\omega(k,\,t_e,\,t_s)]|^{1/2}} \tag{B1}$$

and

$$\sigma_\omega(k,\,t,\,t') = -\omega t - S(k,t,t')\,, \tag{B2}$$

$$S(k,t,t') = \int_{t'}^{t} dt''\Delta\varepsilon_{\kappa(t'')}^{cv}. \tag{B3}$$

The stationary-phase times t_s and t_e are obtained numerically from the saddle-point conditions [15]

$$\Delta\varepsilon_{\kappa(t_s)}^{cv} = 0, \tag{B4}$$

$$\Delta\varepsilon_{\kappa(t_e)}^{cv} = \omega, \tag{B5}$$

where $\kappa(t) = k + A(t)$. We determine the roots t_s by expanding Eq. (B4) in the analytical continuation $K(t)$ of the adiabatic momentum $\kappa(t)$:

$$\Delta\varepsilon_{K(t_s)}^{cv} = \Delta\varepsilon_0^{cv} + \frac{K^2}{2m_0^*} + O(K(t_s)^3). \tag{B6}$$

The truncation of this expansion is justified by interband excitations primarily occurring close to the Γ point. The reduced effective electron-hole-pair mass

$$m_0^* = \frac{m_{vk}^* m_{ck}^*}{m_{vk}^* - m_{ck}^*}|_{k=0}$$

is defined by the valence and conduction band effective masses

$$\frac{1}{m_{nk}^*} = \frac{\partial^2\varepsilon_{nk}}{\partial k^2}, \quad n = v,\ c. \tag{B7}$$

Solving Eq. (B6) for $\tilde{A}(t_s) = \pm i\gamma - k/A_0$, expanding t_s in powers of $\gamma = \sqrt{2m_0^*\Delta\varepsilon_0^{cv}}/A_0$, and using generic properties of the derivative of the inverse of a function, we find

$$t_s = \tilde{A}^{-1}\left(-\frac{k}{A_0}\right) \pm \frac{1}{\omega_0}\left\{\frac{i\gamma}{\tilde{E}[\tilde{A}^{-1}(-k/A_0)]} + O\left(\frac{\gamma^2}{2!}\right)\right\}, \tag{B8}$$

with real and imaginary parts

$$\text{Re}[t_s] = \tilde{A}^{-1}\left(-\frac{k}{A_0}\right) + \frac{1}{\omega_0}O\left(\frac{\gamma^2}{2!}\right), \tag{B9}$$

$$\mathrm{Im}[t_s(k)] = \frac{\pm A_0\gamma}{E[\tilde{A}^{-1}(-k/A_0)]} + O\left(\frac{\gamma^3}{3!}\right) \quad \text{(B10)}$$

$$= \frac{\sqrt{2m_0^*\varepsilon_0^{cv}}}{|E[\mathrm{Re}(t_s)]|} + O\left(\frac{\gamma^3}{\omega_0}\right). \quad \text{(B11)}$$

To arrive at (B11), we used (B9). The magnitude of the electric field in (B11), $|E[\mathrm{Re}(t_s)]|$, indicates that only the regular solution matters [4,59]. Equation (B11) links $\mathrm{Im}(t_s)$ and the instantaneous electric field at the time of excitation $E[\mathrm{Re}(t_s)]$ and is relevant for the discussion of Fig. 6 at the end of Sec. III B. In our numerical applications, we have $\gamma^2/6 \approx 0.16 \leqslant 1$ for $E_0 = 0.11$ V/Å and $\gamma^2/6 \approx 0.09 \leqslant 1$ for $E_0 = 0.15$ V/Å, justifying the truncation of this expansion.

To characterize the dependence of the HH yield

$$Y^{er}(\omega) = \left|\int_{\mathrm{BZ}} dk\, \hat{f}_k^{er}(\omega)\right|^2 \leqslant \left(\int_{\mathrm{BZ}} dk |\hat{f}_k^{er}(\omega)|\right)^2 \quad \text{(B12)}$$

on the electric field of the driving pulse, we note that t_e is real and approximate the integrand in Eq. (B3) by the minimal band-gap energy $\Delta\epsilon_0^{cv}$. We thus replace the exponent in (B1) by its lower limit

$$\mathrm{Im}[S(k, t_e, t_s)] \approx -\Delta\varepsilon_0^{cv}|\mathrm{Im}(t_s)|. \quad \text{(B13)}$$

Designating with $t_s^{\max}(k)$ the root of Eq. (B4) that yields the largest contribution to (B1), defining

$$|\tilde{j}_k^{er}(t_e, t_s)| = e^{\mathrm{Im}[S(k,t_e,t_s)]}|j_k^{er}(t_e, t_s)|,$$

and using Eq. (B13), we find the upper limit for Eq. (B1):

$$\sum_{t_s}\sum_{t_e}|j_k^{er}(t_e, t_s)| \leqslant e^{-\Delta\varepsilon_0^{cv}|\mathrm{Im}(t_s^{\max})|}\sum_{t_e}|\tilde{j}_k^{er}(t_e, t_s^{\max})|. \quad \text{(B14)}$$

Applying Eq. (B10), we obtain for the HH in yield each k channel

$$\sqrt{Y_k^{er}(\omega)} \propto \sum_{t_s}\sum_{t_e}|j_k^{er}(t_e, t_s)|. \quad \text{(B15)}$$

Introducing the crystal momentum with the largest contribution to the integral in Eq. (B12), $k = k_0(R, \tau)$, and defining $t_s^0 = t_s^{\max}(k_0(R, \tau))$, we obtain, according to Eq. (B10),

$$\mathrm{Im}(t_s^0) \geqslant \frac{1}{\omega_0}\frac{\gamma}{\tilde{E}^{\mathrm{peak}}(R, \tau)}.$$

For all k channels this implies that the exponential factor in Eqs. (B14) and (B15) is limited by

$$\exp\left[-\Delta\varepsilon_0^{cv}|\mathrm{Im}(t_s^0)|\right] \leqslant \exp\left[-\frac{\Delta\varepsilon_0^{cv}}{\omega_0}\frac{\gamma}{\tilde{E}^{\mathrm{peak}}(R, \tau)}\right].$$

The k-integrated HH yield is therefore approximately proportional to

$$Y^{er}(\omega) \propto \exp\left[-\frac{\sqrt{8m_0^*}(\Delta\varepsilon_0^{cv})^{3/2}}{E_0\tilde{E}^{\mathrm{peak}}(R, \tau)}\right],$$

where we replaced $\gamma = \sqrt{2m_0^*\Delta\varepsilon_0^{cv}}/A_0$.

Special case: Analytical solution for $\tau = T_{\omega_0}/8$

Under the simplifying assumption of an extended pulse, i.e., by setting $f(t) = g(t) \equiv 1$ in Eqs. (3) and (6), and for the specific value $\tau = T_{\omega_0}/8$ of the chromatic delay, the crystal momentum $k = k_0(R, \tau)$ with the largest contribution to the integral in Eq. (B12) can be approximated in closed analytic form. In this case, we obtain from Eqs. (4), (12), (B4), and (B6)

$$\frac{1}{2m_0^*}[k - A_{0,\omega_0}\sin(\omega_0 t_s) + A_{0,2\omega_0}\cos(2\omega_0 t_s)]^2 = -\Delta\varepsilon_0^{cv}.$$

Since $\cos(2\omega_0 t_s) = 1 - 2\sin^2(\omega_0 t_s)$ this is a quadratic equation. From its four solutions

$$\sin(\omega_0 t_s^\nu) = -\frac{\sqrt{1-R} \pm \sqrt{1+R+4\sqrt{R}(k/A_0 \pm i\gamma)}}{2\sqrt{R}}$$

with $\nu = 1, 2, 3, 4$, we obtain, modulo $2\pi/\omega_0$,

$$\mathrm{Im}\left(t_s^{1,2}\right) = -\frac{\gamma/\omega_0}{\sqrt{4\frac{k}{A_0}\sqrt{R}+R+1}\sqrt{1-\frac{\left(\sqrt{4\frac{k}{A_0}\sqrt{R}+R+1}\mp\sqrt{1-R}\right)^2}{4R}}} + O(\gamma^3),$$

$$\mathrm{Im}\left(t_s^{3,4}\right) = \frac{\gamma/\omega_0}{\sqrt{4\frac{k}{A_0}\sqrt{R}+R+1}\sqrt{1-\frac{\left(\sqrt{4\frac{k}{A_0}\sqrt{R}+R+1}\mp\sqrt{1-R}\right)^2}{4R}}} + O(\gamma^3).$$

To first order in γ, two of these solutions are regular (t_s^3 and t_s^4), of which the solution with the larger imaginary part is $t_s^{\max} = t_s^3$. The crystal momentum k is maximal at

$$k_0\left(R, \frac{T_{\omega_0}}{8}\right) = A_0\frac{3\left(\sqrt{-31R^2+30R+1}+R-1\right)}{32\sqrt{R}}. \quad \text{(B16)}$$

The dependence of $k_0(R, T_{\omega_0}/8)$ on the harmonic conversion parameter R is shown in Fig. 9. As expected [15], for monochromatic driving pulses ($R = 0, 1$) $k_0 = 0$, and the maximum contribution to the HH yield occurs at the Γ point ($k = 0$ channel). In contrast, for the bichromatic driving pulse with $\tau = T_{\omega_0}/8$ and $0 < R < 1$ maximal yield contributions arise at crystal momenta $k \neq 0$ and depend on the driving pulse intensity and R. We expect that a similar effect will occur for other bichromatic pulses with $\tau \neq 0$, due to the broken symmetry of the adiabatic crystal momenta $\kappa(t)$, relative to the Γ point (characterized by asymmetry parameters $\mathcal{A} \neq 0$).

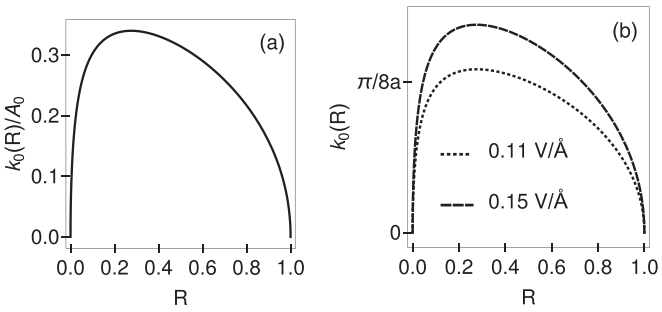

FIG. 9. Initial crystal-momentum channel $|k| = k_0(R)$ with the largest contribution to the interband HH yield as a function of the harmonic conversion parameter R.

APPENDIX C: MODULATION OF THE PLATEAU YIELD WITH *R*

In order to examine the oscillations of interband HH yields in Figs. 7 and 8, we start with the BZ-integrated interband current as given by Eq. (E1) in Ref. [15],

$$\hat{J}^{er}(\omega) \propto \sum_{|k_r|<A^{\rm peak}} \sum_{t_e} \sum_{t_s} j^{er}_{k_r}(t_e, t_s), \tag{C1}$$

where we define

$$j^{er}_l = j^{er}_{k_r}(t_e, t_s) = \frac{E(t_s)e^{i\sigma_\omega(l)}}{|\det[\mathrm{Hess}\sigma_\omega(l)]|^{1/2}}$$

with the collective label $l = (k_r, t_e, t_s)$. t_s, t_e, and k_r are obtained by numerically solving the saddle-point conditions (B4), (B5), and

$$\int_{t_s}^{t_e} dt\left[P^{vv}_{\kappa_r(t)} - P^{cc}_{\kappa_r(t)}\right] = 0, \tag{C2}$$

where

$$P^{nn}_{\kappa(t)} = \frac{1}{a}\int_0^a dx\, \phi^*_{n\kappa(t)}(x)\hat{p}\phi_{n\kappa(t)}(x), \quad n = v, c \tag{C3}$$

are the momentum-operator matrix elements for the valence (v) and lowest conduction (c) band [15,60]. The limits of the sum over k_r are given by the range of initial k channels $|k_r| < A^{\rm peak}(R, \tau)$, that can be translated to the Γ point in the external field.

The saddle-point approximation to the total integrated interband yield is proportional to

$$Y^{er}(\omega) \propto \left|\hat{J}^{er}(\omega)\right|^2 \propto \sum_{l1} |j^{er}_{l1}|^2 + 2\sum_{l1}\sum_{l2<l1} j^{er}_{l1,l2}(\omega).$$

The interference term

$$j^{er}_{l1,l2}(\omega) = \frac{e^{\mathrm{Im}(S_1+S_2)}|E(t_{s1})E(t_{s2})|\cos(S_{\rm int})}{|\det[\mathrm{Hess}\sigma_\omega(l1)]\det[\mathrm{Hess}\sigma_\omega(l2)]|^{1/2}}$$

includes contributions to the HH yield from different electron trajectories that are excited to the conduction band at the same times $t_{e1} = t_{e2} = t_e$. It is written in terms of the action (B3) and phase difference

$$S_{\rm int} = \mathrm{Re}[S(k_{r2}, t_e, t_{s2}) - S(k_{r1}, t_e, t_{s1})] + \chi,$$
$$\chi = \arg[E(t_{s1})] - \arg[E(t_{s2})].$$

Its 2π periodicity in the phase $S_{\rm int}$ is the cause of the observed R oscillations of the HH yields, as we will show next.

Rewriting

$$\mathrm{Re}[S(k_{r2}, t_e, t_{s2}) - S(k_{r1}, t_e, t_{s1})] = I_{a,2} - I_{a,1} + I_{b,2} - I_{b,1},$$

we separately evaluate the integrals

$$I_{a,j} = \int_{\mathrm{Re}[t_{sj}]}^{t_e} dt\, \Delta\varepsilon^{cv}_{\kappa_{rj}(t)}, \; I_{b,j} = \mathrm{Re}\left\{\int_{t_{sj}}^{\mathrm{Re}[t_{sj}]} dt\, \Delta\varepsilon^{cv}_{\kappa_{rj}(t)}\right\},$$

employing different parametrizations for the active electron's energy. For evaluating $I_{b,j}$ we use a parametrization that accurately describes $\Delta\varepsilon^{cv}_k$ near the Γ point [Eq. (B6)] because electrons are promoted to the conduction band [see Eq. (B4)] primarily with close-to-zero crystal momentum. For solving $I_{a,j}$, we need a parametrization that gives a good overall agreement for crystal momenta in the entire first BZ since, according to Eq. (B5) and for sufficiently high peak intensities, plateau harmonics occur in the spectral range $\Delta\varepsilon^{vc}_0 < \omega < \Delta\varepsilon^{vc}_{\pi/a}$ for adiabatic crystal momenta $|\kappa| \leqslant \pi/(a)$ centered at $\pi/(2a)$.

To evaluate the real integral $I_{a,j}$, selecting an integration path along the real axis, we parametrize the local band-gap energy as

$$\begin{aligned}\Delta\varepsilon^{cv}_\kappa &= \Delta\varepsilon^{cv}_0 + (\Delta_v + \Delta_c)\sin^2(a\kappa/2)\\ &= \Delta\varepsilon^{cv}_0 + \frac{\Delta_v + \Delta_c}{2}\left(1 + |a\kappa| - \frac{\pi}{2}\right)\\ &\quad + O\left[\left(|a\kappa| - \frac{\pi}{2}\right)^3\right],\end{aligned}$$

where Δ_v and Δ_c are the widths of the valence and conduction bands, respectively. Truncating the Taylor expansion about $|a\kappa| = \pi/2$ at the third order, we find

$$\begin{aligned}I_{a,2} - I_{a,1} \approx \mathrm{Re}(t_{s1} - t_{s2})&\left[\Delta\varepsilon^{cv}_0 + \frac{\Delta_v + \Delta_c}{2}\left(1 - \frac{\pi}{2}\right)\right]\\ &+ \frac{a(\Delta_v + \Delta_c)}{2}\left[\int_{\mathrm{Re}[t_{s2}]}^{t_e} dt|k_{r2} + A(t)|\right.\\ &\left. - \int_{\mathrm{Re}[t_{s1}]}^{t_e} dt|k_{r1} + A(t)|\right]\end{aligned}$$

and

$$\begin{aligned}|I_{a,2} - I_{a,1}| \leqslant |\mathrm{Re}(t_{s1} - t_{s2})|&\left|\Delta\varepsilon^{cv}_0 + \frac{\Delta_v + \Delta_c}{2}\left(1 - \frac{\pi}{2}\right)\right|\\ &+ \frac{a(\Delta_v + \Delta_c)}{2}\left[\left|\int_{\mathrm{Re}[t_{s2}]}^{\mathrm{Re}[t_{s1}]} dt|A(t)|\right|\right.\\ &\left. + |t_e - \mathrm{Re}(t_{s2})||k_{r2}| + |\mathrm{Re}(t_{s1}) - t_e||k_{r1}|\right]\end{aligned}$$

by using the inequality $|k_{rj} + A(t)| \leqslant |k_{rj}| + |A(t)|$. Since $A(t) \leqslant A_0\tilde{A}^{\rm peak}(R, \tau)$, we have the upper limit

$$\left|\int_{\mathrm{Re}[t_{s2}]}^{\mathrm{Re}[t_{s1}]} dt|A(t)|\right| \leqslant |\mathrm{Re}[t_{s1}] - \mathrm{Re}[t_{s2}]|A_0\tilde{A}^{\rm peak}(R, \tau).$$

Thus, due to

$$|\mathrm{Re}(t_{s1}) - t_e|, |t_e - \mathrm{Re}(t_{s2})|, |\mathrm{Re}(t_{s2} - t_{s1})| \leqslant T_{\omega_0},$$

we obtain

$$\begin{aligned}|I_{a,2} - I_{a,1}| \leqslant T_{\omega_0}\Delta\varepsilon^{cv}_0&\left\{1 + \frac{\Delta_v + \Delta_c}{2\Delta\varepsilon^{cv}_0}\left[1 - \frac{\pi}{2}\right.\right.\\ &\left.\left. + a(A_0\tilde{A}^{\rm peak}(R, \tau) + |k_{r1}| + |k_{r2}|)\right]\right\}.\end{aligned} \tag{C4}$$

Next, by replacing Eq. (B6) in the integrand of $I_{b,i}$, we find

$$|I_{b,i}| = \left|\frac{A_0^2}{m_0^*}\int_0^{\mathrm{Im}[t_{si}]} dl\big[\mathrm{Re}[\tilde{A}(t_{si})] - \mathrm{Re}\{\tilde{A}[\mathrm{Re}(t_{si}) + il]\}\big]\,\mathrm{Im}\{\tilde{A}[\mathrm{Re}(t_{si}) + il]\}\right|$$
$$\leqslant T_{\omega_0}\Delta\varepsilon_0^{cv}\left|\frac{\tilde{\dot{E}}[\mathrm{Re}(t_{si})]\gamma^2}{2\pi\tilde{E}^3[\mathrm{Re}(t_{si})]} + O(\gamma^4)\right|. \tag{C5}$$

Here, $\tilde{\dot{E}}[\mathrm{Re}(t_{si})]$ is the normalized derivative of the field strength, defined in analogy to Eq. (14). The remaining term can be calculated as

$$\arg[E(t_{si})] = \arctan\left\{\frac{\mathrm{Im}[E(t_{si})]}{\mathrm{Re}[E(t_{si})]}\right\}$$
$$= \frac{\tilde{\dot{E}}[\mathrm{Re}(t_{si})]}{\tilde{E}^2[\mathrm{Re}(t_{si})]}\gamma + O(\gamma^3). \tag{C6}$$

In deriving this equation, we used

$$\mathrm{Re}[\tilde{E}(t_{si})] = \tilde{E}[\mathrm{Re}(t_{si})] + O[\mathrm{Im}(t_{si})^2],$$

$$\mathrm{Im}[\tilde{E}(t_{si})] = \omega_0\tilde{\dot{E}}[\mathrm{Re}(t_{si})]\mathrm{Im}(t_{si}) + O[\mathrm{Im}(t_{si})^3],$$

and truncated the expansion of $\arctan\{\frac{\mathrm{Im}[E(t_{si})]}{\mathrm{Re}[E(t_{si})]}\}$ according to $\arctan(x) = x + O(x^3)$. Finally, keeping the lowest order of Eqs. (C5) and (C6), we find the approximate upper limit

$$|S_{\mathrm{int}}| \leqslant |I_{a,2} - I_{a,1}| + |I_{b,2}| + |I_{b,1}| + |\chi|$$
$$\leqslant |I_{a,2} - I_{a,1}| + T_{\omega_0}\Delta\varepsilon_0^{cv}\left\{\left|\frac{\tilde{\dot{E}}[\mathrm{Re}(t_{s2})]}{\tilde{E}^3[\mathrm{Re}(t_{s2})]}\right| + \left|\frac{\tilde{\dot{E}}[\mathrm{Re}(t_{s1})]}{\tilde{E}^3[\mathrm{Re}(t_{s1})]}\right|\right\}\frac{\gamma^2}{2\pi} + \left|\frac{\tilde{\dot{E}}[\mathrm{Re}(t_{s2})]}{\tilde{E}^2[\mathrm{Re}(t_{s2})]} - \frac{\tilde{\dot{E}}[\mathrm{Re}(t_{s1})]}{\tilde{E}^2[\mathrm{Re}(t_{s1})]}\right|\gamma.$$

Numerical values are $\gamma/(T_{\omega_0}\Delta\varepsilon_0^{cv}) \approx 0.015$ for $E_0 = 0.11$ V/Å and $\gamma/(T_{\omega_0}\Delta\varepsilon_0^{cv}) \approx 0.011$ for $E_0 = 0.15$ V/Å. On the other hand, $\gamma^2/2\pi \approx 0.16$ for $E_0 = 0.11$ V/Å and $\gamma^2/2\pi \approx 0.09$ for $E_0 = 0.15$ V/Å. We can thus approximate dominant variation of S_{int} with R by the upper limit given in (C4):

$$S_{\mathrm{int}} \propto |I_{a,2} - I_{a,1}|.$$

The R-modulation period corresponds to a phase change of 2π of S_{int}:

$$\delta S_{\mathrm{int}} = \frac{\partial(S_{\mathrm{int}})}{\partial R}\delta R = 2\pi.$$

Thus, neglecting the dependence of $|k_{rj}|$ on R, the period of the HH yield oscillation with R is approximately

$$\delta R \propto \frac{\omega_0^2}{E_0}\left[\frac{a(\Delta_v + \Delta_c)}{2}\frac{\partial\tilde{A}^{\mathrm{peak}}(R,\tau)}{\partial R}\right]^{-1}.$$

It decreases for increasing field strengths E_0 of the fundamental-frequency pulse. The R-oscillation periods for different values of E_0, $E_{0,1}$, and $E_{0,2}$ are related as

$$\frac{\delta R_1}{\delta R_2} \approx \frac{E_{0,1}}{E_{0,2}}. \tag{C7}$$

[1] M. Ferray, A. L'Huillier, X. F. Li, L. A. Lompre, G. Mainfray, and C. Manus, J. Phys. B: At., Mol. Opt. Phys. **21**, L31 (1988).
[2] J. L. Krause, K. J. Schafer, and K. C. Kulander, Phys. Rev. Lett. **68**, 3535 (1992).
[3] P. B. Corkum, Phys. Rev. Lett. **71**, 1994 (1993).
[4] M. Lewenstein, P. Balcou, M. Y. Ivanov, A. L'Huillier, and P. B. Corkum, Phys. Rev. A **49**, 2117 (1994).
[5] A.-T. Le, R. R. Lucchese, S. Tonzani, T. Morishita, and C. D. Lin, Phys. Rev. A **80**, 013401 (2009).
[6] F. Krausz and M. Ivanov, Rev. Mod. Phys. **81**, 163 (2009).
[7] L. Plaja and L. Roso-Franco, Phys. Rev. B **45**, 8334 (1992).
[8] M. Protopapas, C. H. Keitel, and P. L. Knight, Rep. Prog. Phys. **60**, 389 (1997).
[9] F. H. M. Faisal and J. Z. Kamiński, Phys. Rev. A **54**, R1769(R) (1996).
[10] F. H. M. Faisal and J. Z. Kamiński, Phys. Rev. A **56**, 748 (1997).
[11] S. Ghimire, A. D. DiChiara, E. Sistrunk, P. Agostini, L. F. DiMauro, and D. A. Reis, Nat. Phys. **7**, 138 (2011).
[12] M. Wu, S. Ghimire, D. A. Reis, K. J. Schafer, and M. B. Gaarde, Phys. Rev. A **91**, 043839 (2015).
[13] G. Vampa, C. R. McDonald, G. Orlando, D. D. Klug, P. B. Corkum, and T. Brabec, Phys. Rev. Lett. **113**, 073901 (2014).
[14] J. Li, S. Fu, H. Wang, X. Zhang, B. Ding, B. Hu, and H. Du, Phys. Rev. A **98**, 043409 (2018).
[15] F. Navarrete, M. F. Ciappina, and U. Thumm, Phys. Rev. A **100**, 033405 (2019).
[16] S. Ghimire and D. Reis, Nat. Phys. **15**, 10 (2019).

[17] G. Vampa, C. R. McDonald, G. Orlando, P. B. Corkum, and T. Brabec, Phys. Rev. B **91**, 064302 (2015).

[18] E. N. Osika, A. Chacón, L. Ortmann, N. Suárez, J. A. Pérez-Hernández, B. Szafran, M. F. Ciappina, F. Sols, A. S. Landsman, and M. Lewenstein, Phys. Rev. X **7**, 021017 (2017).

[19] G. Ndabashimiye, S. Ghimire, M. Wu, D. A. Browne, K. J. Schafer, M. B. Gaarde, and D. A. Reis, Nature (London) **534**, 520 (2016).

[20] A. J. Uzan, G. Orenstein, Á. Jiménez-Galán, C. McDonald, R. E. F. Silva, B. D. Bruner, N. D. Klimkin, V. Blanchet, T. Arusi-Parpar, M. Krüger *et al.*, Nat. Photonics **14**, 183 (2020).

[21] S. R. Leone, C. W. McCurdy, J. Burgdörfer, L. S. Cederbaum, Z. Chang, N. Dudovich, J. Feist, C. H. Greene, M. Ivanov, R. Kienberger *et al.*, Nat. Photonics **8**, 162 (2014).

[22] F. Calegari, G. Sansone, S. Stagira, C. Vozzi, and M. Nisoli, J. Phys. B: At. Mol. Opt. Phys. (topical review) **49**, 062001 (2016).

[23] Z. Chang, P. B. Corkum, and S. R. Leone, J. Opt. Soc. Am. B **33**, 1081 (2016).

[24] M. J. Ambrosio and U. Thumm, Phys. Rev. A **100**, 043412 (2019).

[25] U. Thumm, Q. Liao, E. M. Bothschafter, F. Süßmann, M. F. Kling, and R. Kienberger, *Attosecond Physics: Attosecond Streaking Spectroscopy of Atoms and Solids* (Wiley, Hoboken, NJ, 2015), Chap. 13, pp. 387–441.

[26] M. Nisoli, P. Decleva, F. Calegari, A. Palacios, and F. Martín, Chem. Rev. **117**, 10760 (2017).

[27] J. Li, E. Saydanzad, and U. Thumm, Phys. Rev. A **95**, 043423 (2017).

[28] J. Li, E. Saydanzad, and U. Thumm, Phys. Rev. Lett. **120**, 223903 (2018).

[29] Q. Liao, W. Cao, Q. Zhang, K. Liu, F. Wang, P. Lu, and U. Thumm, Phys. Rev. Lett. **125**, 043201 (2020).

[30] T. T. Luu and H. J. Wörner, Phys. Rev. B **94**, 115164 (2016).

[31] F. Krausz and M. I. Stockman, Nat. Photonics **8**, 205 (2014).

[32] N. Dudovich, O. Smirnova, J. Levesque, Y. Mairesse, M. Y. Ivanov, D. M. Villeneuve, and P. B. Corkum, Nat. Phys. **2**, 781 (2006).

[33] G. Vampa, T. J. Hammond, N. Thire, B. E. Schmidt, F. Legare, C. R. McDonald, T. Brabec, and P. B. Corkum, Nature (London) **522**, 462 (2015).

[34] T. T. Luu and H. J. Wörner, Phys. Rev. A **98**, 041802(R) (2018).

[35] H. Shirai, F. Kumaki, Y. Nomura, and T. Fuji, Opt. Lett. **43**, 2094 (2018).

[36] G. Vampa, T. J. Hammond, N. Thiré, B. E. Schmidt, F. Légaré, C. R. McDonald, T. Brabec, D. D. Klug, and P. B. Corkum, Phys. Rev. Lett. **115**, 193603 (2015).

[37] D. Peng, M. V. Frolov, L.-W. Pi, and A. F. Starace, Phys. Rev. A **97**, 053414 (2018).

[38] M. V. Frolov, N. L. Manakov, A. A. Minina, N. V. Vvedenskii, A. A. Silaev, M. Y. Ivanov, and A. F. Starace, Phys. Rev. Lett. **120**, 263203 (2018).

[39] J.-B. Li, X. Zhang, S.-J. Yue, H.-M. Wu, B.-T. Hu, and H.-C. Du, Opt. Express **25**, 18603 (2017).

[40] M. V. Frolov, N. L. Manakov, A. A. Minina, A. A. Silaev, N. V. Vvedenskii, M. Y. Ivanov, and A. F. Starace, Phys. Rev. A **99**, 053403 (2019).

[41] M. Mofared, E. Irani, and R. Sadighi-Bonabi, Phys. Chem. Chem. Phys. **21**, 9302 (2019).

[42] X. Song, S. Yang, R. Zuo, T. Meier, and W. Yang, Phys. Rev. A **101**, 033410 (2020).

[43] T.-J. Shao, L.-J. Lü, J.-Q. Liu, and X.-B. Bian, Phys. Rev. A **101**, 053421 (2020).

[44] D. Ray, F. He, S. De, W. Cao, H. Mashiko, P. Ranitovic, K. P. Singh, I. Znakovskaya, U. Thumm, G. G. Paulus *et al.*, Phys. Rev. Lett. **103**, 223201 (2009).

[45] J. Wu, M. Magrakvelidze, L. Schmidt, M. Kunitski, T. Pfeifer, M. Schöffler, M. Pitzer, M. Richter, S. Voss, H. Sann *et al.*, Nat. Commun. **4**, 2177 (2013).

[46] J. Wu, M. Kunitski, M. Pitzer, F. Trinter, L. Schmidt, T. Jahnke, M. Magrakvelidze, C. Madsen, L. Madsen, U. Thumm *et al.*, Phys. Rev. Lett. **111**, 023002 (2013).

[47] M. Magrakvelidze and U. Thumm, Phys. Rev. A **88**, 013413 (2013).

[48] S. Skruszewicz, J. Tiggesbäumker, K.-H. Meiwes-Broer, M. Arbeiter, T. Fennel, and D. Bauer, Phys. Rev. Lett. **115**, 043001 (2015).

[49] T. Paschen, M. Förster, M. Krüger, C. Lemell, G. Wachter, F. Libisch, T. Madlener, J. Burgdörfer, and P. Hommelhoff, J. Mod. Opt. **64**, 1054 (2017).

[50] R. W. Boyd, *Nonlinear Optics* (Academic, New York, 2003).

[51] M. Wu, D. A. Browne, K. J. Schafer, and M. B. Gaarde, Phys. Rev. A **94**, 063403 (2016).

[52] R. D. L. Kronig, W. G. Penney, and R. H. Fowler, Proc. R. Soc. London A **130**, 499 (1931).

[53] P. Atkins and R. Friedman, *Molecular Quantum Mechanics* (Oxford University Press, Oxford, 2005).

[54] L. Li, P. Lan, X. Zhu, T. Huang, Q. Zhang, M. Lein, and P. Lu, Phys. Rev. Lett. **122**, 193901 (2019).

[55] Y.-N. Xu and W. Y. Ching, Phys. Rev. B **43**, 4461 (1991).

[56] F. Tran and P. Blaha, Phys. Rev. Lett. **102**, 226401 (2009).

[57] Y. S. You, D. A. Reis, and S. Ghimire, Nat. Phys. **13**, 345 (2017).

[58] D. J. Griffiths, *Introduction to Electrodynamics* (Prentice Hall, Upper Saddle River, NJ, 1999).

[59] D. B. Miloševic, G. G. Paulus, and W. Becker, Phys. Rev. Lett **89**, 153001 (2002).

[60] U. Lindefelt, H.-E. Nilsson, and M. Hjelm, Semicond. Sci. Technol. **19**, 1061 (2004).